Appendix E
FCT Document Cover Sheet

Name/Title of Deliverable/Milestone	Final Report
Work Package Title and Number	Project 13-5505: Mechanical Behavior of UO2 at Sub-grain Length Scales: Quantification of Elastic, Plastic and Creep Properties via Microscale Testing
Work Package WBS Number	NU-13-AZ-ASU_-0101-05
Responsible Work Package Manager	Pedro Peralta / Pedro D. Peralta (Name/Signature)
Date Submitted	4/16/18

Quality Rigor Level for Deliverable/Milestone	☒ QRL-3	☐ QRL-2	☐ QRL-1 ☐ Nuclear Data	☐ N/A*

This deliverable was prepared in accordance with University of California Berkeley
(Participant/National Laboratory Name)

QA program which meets the requirements of
☒ DOE Order 414.1 ☐ NQA-1-2000

This Deliverable was subjected to:

☒ Technical Review ☐ Peer Review

Technical Review (TR)
Review Documentation Provided
☐ Signed TR Report or,
☐ Signed TR Concurrence Sheet or,
☒ Signature of TR Reviewer(s) below

Peer Review (PR)
Review Documentation Provided
☐ Signed PR Report or,
☐ Signed PR Concurrence Sheet or,
☐ Signature of PR Reviewer(s) below

Name and Signature of Reviewers

J. Rajagopalan R. Jagopalan

*Note: In some cases there may be a milestone where an item is being fabricated, maintenance is being performed on a facility, or a document is being issued through a formal document control process where it specifically calls out a formal review of the document. In these cases, documentation (e.g., inspection report, maintenance request, work planning package documentation or the documented review of the issued document through the document control process) of the completion of the activity along with the Document Cover Sheet is sufficient to demonstrate achieving the milestone. QRL for such milestones may be also be marked N/A in the work package provided the work package clearly specifies the requirement to use the Document Cover Sheet and provide supporting documentation.

Mechanical Behavior of UO_2 at Sub-Grain Length Scales: Quantification of Elastic, Plastic and Creep Properties via Microscale Testing

B. Shaffer, K. Roney, B. Gong, H. Lim, R. McDonald, K. Rudman, and P. Peralta

Arizona State University (ASU)

D. Frazer and P. Hosemann

University of California, Berkeley (UCB)

Award # DE-NE0000670

PICSNE Work Package #: NU-13-AZ-ASU-0101-05

Final Report

Reporting Period: December 2013-December 2017

Mechanical Behavior of UO_2 at Sub-Grain Length Scales: Quantification of Elastic, Plastic and Creep Properties via Microscale Testing

Summary

Techniques were developed to measure properties at sub-grain scales using depleted Uranium Oxide (d-UO2) samples heat-treated to obtain different grain sizes and oxygen stoichiometries, through three main tasks: 1) sample processing and characterization, 2) microscale and conventional testing and 3) modeling. Grain size and crystallography were characterized using Scanning Electron Microscopy (SEM), in conjunction with Electron Backscattering Diffraction (EBSD) and Electron Channeling Contrast Imaging (ECCI). Grains were then carefully selected based on their crystallographic orientations to perform ex-situ micromechanical tests with samples machined via Focused Ion Beam (FIB), with emphasis on micro-cantilever bending. These experiments were performed under controlled atmospheres, to insure stoichiometry control, at temperatures up to 700 °C and allowed measurements involving elastic (effective Young's modulus), plastic (critical resolved shear stresses) and creep (creep strain rates) behavior. Conventional compression experiments were performed simultaneously to compare with the ex-situ measurements and study potential size effects. Modeling was implemented using anisotropic elasticity and inelastic constitutive relations for plasticity and creep based on kinematics and kinetics of dislocation glide that account for the effects of crystal orientation, and stress. The models will be calibrated and validated using the experimental data. This project provided insight on correlations among stoichiometry, crystallography and mechanical behavior in advanced oxide fuels, provided valuable experimental data to validate and calibrate meso-scale fuel performance codes and also a framework to measure sub-grain scale mechanical properties that should be suitable for use with irradiated samples due to small volumes required.

The goals and metrics of the ongoing study of thermo-mechanical behavior in depleted uranium dioxide (d-UO_2) outlined in this project have been concluded successfully, resulting in: 1) the successful fabrication, processing, and characterization of large-grained samples with various orientations (up to and including single crystals) having stoichiometric and hyper-stoichiometric O/U ratios; 2) formulation, calibration, and validation of a crystal plasticity constitutive model to describe the creep deformation of UO_2 at the sub-grain length scale (single crystal level) at intermediate temperatures; 3) the successful calibration of a crystal plasticity constitutive model to describe the elasto-plastic deformation of microcantilever beams, also at moderate temperatures. Samples were prepared from natural uranium oxide powder of production-quality provided by Areva. The powder was pressed in a die to a pressure of 100 MPa to produce green pellets with no sintering aids, lubricants, or any other additives. The green pellets were then heated up to 1700 °C under ultra-high purity argon atmosphere (~1 ppm O_2). The atmosphere was then changed to 79% Argon, 21% O_2 and the temperature was held at 1700 °C for 2 hours to sinter the pellets under oxidative conditions [1] that are known to increase grain growth kinetics in UO_2 [2]. Samples were then cooled down under Ar-4%H_2 atmosphere to reduce the samples back to stoichiometric UO_2.

For macro-scale procedures, testing of UO_2 samples with large grains was performed at 1200 °C using a modified load frame capable of applying dead-weight loads to ensure constant stress conditions, while displacement of the sample produced by the applied load was measured with high precision micrometers to obtain strains. Stress steps were used during testing and the strains

were monitored to measured creep strain rates under steady state for each level of stress used, so that stress exponents could be obtained. The results of the mechanical testing, along with sample geometry and crystal orientation of the grains in the samples, as well as post-test sample characterization were used to formulate a viscoplastic model to account for steady state (stage II) creep behavior, along with basic assumptions from crystal plasticity and kinematic constraints due to testing fixtures.

In the micro-scale, testing of microcantilever beams at temperatures ranging from 25 to 570 °C was performed in-situ with a scanning electron microscope with a special attachment to apply load and measure displacement while the samples were at temperature. The load-displacement curves obtained showed linear behavior before fracture for all temperatures attempted except 570 °C, where clear deviations from non-linearity were observed before fracture. These deviations were consistently observed for all samples tested for a given orientation. A viscoplastic model was used to account for the presence of inelastic strain, along with basic assumptions from crystal plasticity and beam theory. These models were kept as simple as possible, and results from tests performed in a set of samples with a given crystal orientation were used to calibrate the material constants for the model, while results from a different sample set were then used for validation, thus satisfying the conditions of all main tasks within the parameters of this project. Details of these efforts are outlined in this report.

Objectives

• Perform micro- and macro-scale mechanical testing of depleted uranium oxide samples under atmospheres with controlled partial pressures of oxygen.

• Develop techniques to derive sub-grain (single crystal) level mechanical properties from micro- and macro-scale mechanical test results through correlations with crystal orientation of individual grains.

• Characterize deformed samples via SEM and transmission electron microscopy (TEM) to elucidate deformation mechanisms at the sub-grain level, including plasticity and creep.

• Develop a constitutive framework based on the experimental results to model elastic, plastic and creep deformation of UO_2 at the sub-grain level.

Status

1. Experimental

1.1. Sample Processing and Characterization

1.1.1. Heat Treatment Procedure

Main task 1 required the development of facilities and procedures at ASU to produce suitable UO_2 specimens to be used in instrumented macro- and micro-scale testing required for task 2. Data would be collected from these procedures for the purposes of 1) studying thermo-mechanical response, and 2) building the experimental dataset to be used to calibrate and validate computational models, satisfying main task 3. Initial efforts involved heat treatment procedures on previously sintered pellets, generously provided by Los Alamos National Laboratory (LANL), to grow grains sufficiently large as required to meet planned project deliverables; these experiments were successful in producing large-grained samples but were found to be unsuitable for the purposes of this project due to excessive evaporative mass losses and long processing times (results summarized next). Those procedures were later revised to

include full lab-scale production of sintered pellets in the PI's lab at ASU, as early results directed a logistical shift in focus from heat treatment of previously sintered material to pressing and sintering of raw feedstock powder to fully exploit the abnormal grain growth mechanism inherent to oxidative sintering. These later efforts proved successful, providing sample sets of sufficient size for testing, thus satisfying the requirements of Main Task 1.

Initial procedures: Development of facilities for heat treatment of d-UO_2.
Samples with large grain size were needed to accomplish the goals of this project. Hence, the development of heat treatments to produce these samples was of utmost importance. In this case, it was known that UO_2 heat treated under very high oxygen partial pressures (pO_2 ~0.2 atm) at high temperatures (up to 1700 °C) showed very rapid grain growth [2], but the temperatures required surpassed the limits of the initial setup available and was also shown to cause volatilization of uranium oxide [2], which increases the possibility of radioactive contamination. Furthermore, the grain sizes required to machine micro-cantilever beams was not as large as those reported in [2] and the presence of abnormal grain growth reported by these authors was initially thought to be a problem for this work, as many grains with different orientations were needed to obtain reliable statistics. On the other hand, Mansouri and Olander [3] reported significant grain growth in hyper-stoichiometric UO_2 heat-treated at 1200 °C after being irradiated to a burnup of ~10^{-8} fraction of initial metal atom (FIMA). Given this low value of burnup, it was expected that un-irradiated samples would behave somewhat similarly. Based on the kinetic equations provided in [3] a 5-hour heat treatment at 1250 °C would have resulted in grain growth from an initial grain size of ~8 μm to a final grain size of ~10 μm for an oxygen to metal ratio (O/M) of 2.2. Hence, heat treatments at temperatures lower than those used by [2] were performed to study grain growth kinetics under those conditions and evaluate their possible use in specimen production for the purposes of this work.
Unfortunately, readings from the sample thermocouple used during the experiments were interrupted during the heating ramp due to thermocouple failure; subsequent experiments revealed actual sample temperatures being closer to 1100 °C. In the work by Assman et al. [4], microstructural changes were observed depending on the initial stoichiometry and phases present on the sample; the authors proposed low temperature heat treatments to vary microstructure in UO_2, the results of which were somewhat similar to those obtained in these initial procedures. An example of before and after EBSD maps for the first heat treatment that shows evidence of grain motion is provided in **Fig. 1**.

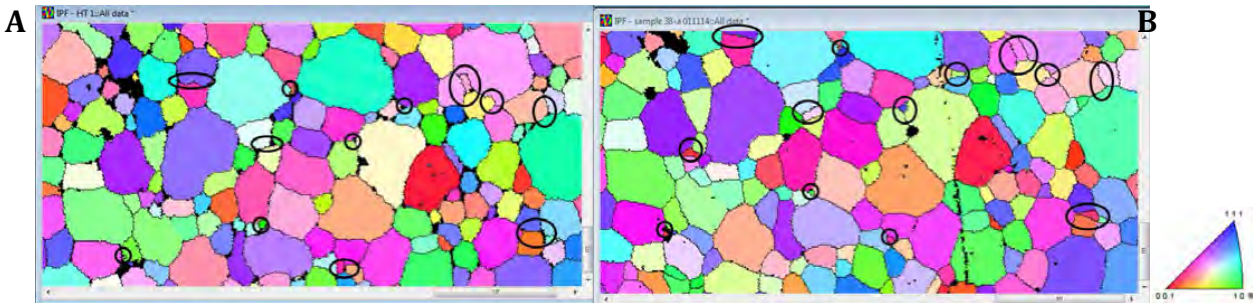

Fig 1. Inverse pole figure (IPF) maps with details of microstructural changes in a UO_2 sample after one cycle of heat treatment at 1100 °C and pO_2 ~ 7x10^{-7} atm. **A**) IPF map of the initial microstructure, and **B**) IPF map of the final microstructure. Regions where changes were found are marked by ellipses. Grain colors represent their out-of-plane crystallographic directions as per the standard triangle in the inset.

The changes in grain size distribution described above suggested that the conditions used tend to homogenize the grain size and would not lead to meaningful increases on average grain size. The overall trend indicated that higher temperatures and O/M values would be needed to increase the average grain size to the larger values needed. Experiments were attempted to increase the sample temperature to the initially planned value of 1250 °C and higher, however, the water-cooled endcaps used for the alumina tube were reaching temperatures close to 100 °C, with the potential danger of explosive expansion of water vapor inside the water lines. Revisions were planned, but the furnace was damaged before they could be implemented. While the damaged furnace underwent repairs, a smaller furnace (rated for 1250 °C) was installed in its place; the revised system was expected to reach sample temperatures at or near 1200 °C using a smaller diameter alumina tube along with alumina heat shields; the resulting pO_2 of ~10^{-4} atm should have led to an oxygen to metal ratio (O/M) of about 2.22 according the phase diagram reported in [1], as shown in **Fig. 2A**. The first procedure with the revised system resulted in a net decrease in average grain size, from 12 µm to about 9.9 µm, with a resulting microstructure that was bimodal, with clusters of small and large grains, as shown in **Fig. 2B**.

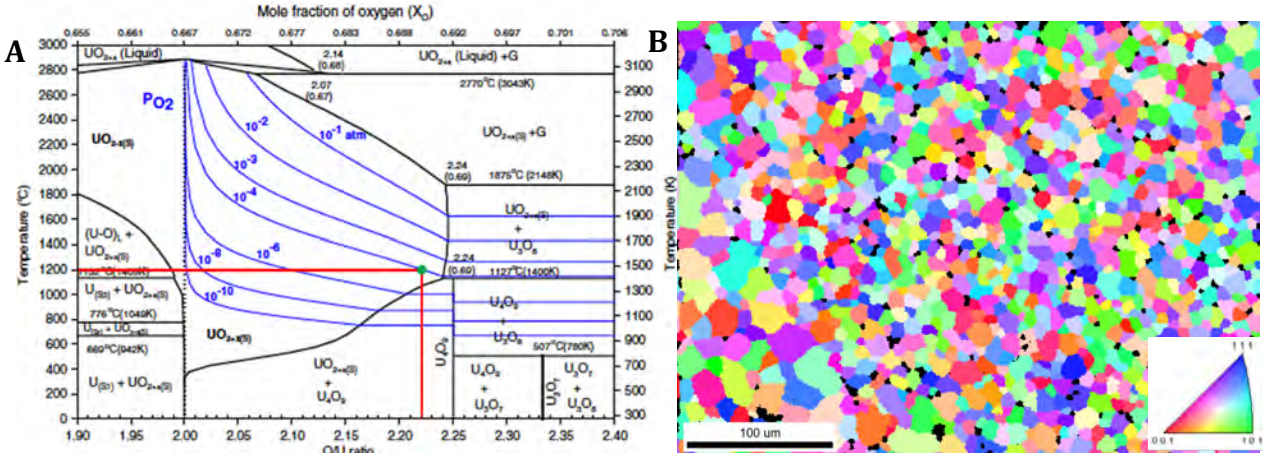

Fig. 2. **A**) Phase diagram of the U-O system [1] showing the conditions for heat treatmen (HT) 3, indicated by the green dot. **B**) Inverse pole figure (IPF) map of the microstructure of a UO_2 sample after HT 3a (nominal conditions: 48 hours at 1200 °C and pO_2 ~ 10^{-4} atm).

That result strongly suggested that the conditions used were too close to the boundary between the UO_{2+x} one-phase region and the UO_{2+x}/U_3O_8 two-phase region, and the low slope of the pO_2 isobars in the phase diagram close to the phase boundary could lead to a transition into the two-phase region given any slight increase in pO_2, due to, for example, small variations in pressure or unexpected sources of oxygen. The transition to the two-phase region can lead to nucleation and growth of a second phase, which combined with the slower kinetics expected at 1200 °C, could lead to some grain growth in the retained UO_{2+x} (larger grains), and some growth of the second phase (smaller grains). Adjustments made for HT 3 (**Fig. 3A**, red lines) resulted in a net increase in grain size from 9.9 µm to 13 µm in number average (used in prior reports) and an area average distribution peak at 15 µm (to be used from this point forward). The predicted grain sizes from the kinetic equations reported in [3] were 13 µm for $UO_{2.08}$ and 27 µm for $UO_{2.2}$, given the time and temperatures used. Discrepancies were attributed to slower oxidation kinetics than expected, which would lead to a shorter "effective" heat treatment time at the desired stoichiometry (~$UO_{2.15}$). The clearest conclusion from those efforts was that the kinetics of grain growth and oxidation at those temperatures (≤1220 °C) were too slow for the purposes of this work.

Intermediate procedures: heat treatment of d-UO_2 at higher temperatures.
The system was revised once more, using a larger furnace with SiC heating elements capable of reaching 1500 °C during quarter 5. Procedure 4 was carried out using the same process atmosphere from previous heat treatments (**Fig. 3A**, blue lines) and resulted in a net increase in grain size (from 15.0 µm to 25.0 µm, area average) as shown in **Fig. 3A/B**.

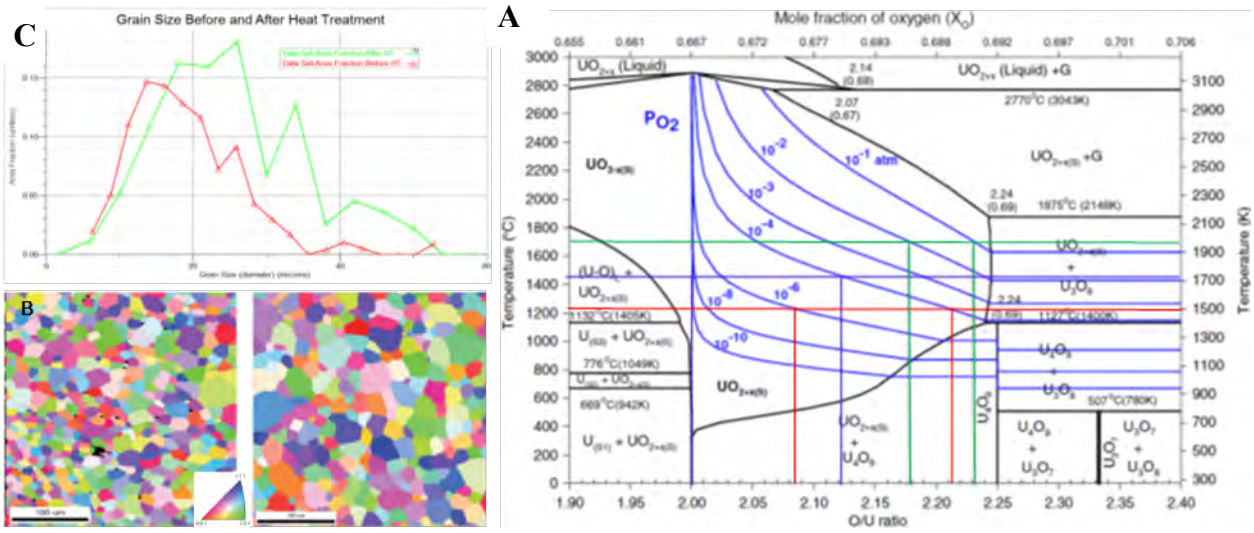

Fig. 3. **A**) Phase diagram of the U-O system [1] showing various heat treatment conditions: 1250 °C furnace (red lines), 1500 °C furnace (blue lines), and 1750 °C furnace (green lines). **B**) Inverse pole figure (IPF) maps of the microstructure of a UO_2 sample, before (A) and after (B) H.T. 4 (76 hours at 1460 °C and $pO_2 \sim 10^{-4}$ atm). **C**) Area fraction data for grain size from EBSD analysis of the UO_2 sample (A) before and (B) after Q5 heat treatment (76 hours at 1460 °C and $pO_2 \sim 10^{-4}$ atm).

The predicted grain sizes for this procedure using the kinetic equations from [3] are 38 µm for $UO_{2.08}$ and 67 µm for $UO_{2.20}$; discrepancies in this experiment were attributed to reduction under the Ar-5% H_2 atmosphere during the ramp to maximum temperature leading to slower initial oxidation kinetics at the time of transition between gases and a greater deviation from the desired stoichiometry at the start of the oxidation phase than expected, leading to a shorter "effective" heat treatment time at the desired stoichiometry (~$UO_{2.12}$). A third treatment gas was added to the alleviate this, consisting of UHP argon (~1 ppm O_2) with an oxygen trap capable to delivering an output stream of Ar-15 ppb O_2 and allowing for an oxygen partial pressure 10^{-8} atm; this was to be used in place of the Ar-5% H_2 during the ramp-up phase to avoid reducing the sample prior to the start of the oxidation phase. The resulting HT 5, slated to last for 192 hours, was shortened by one day due to a thermocouple failure, highlighting the need to shorten processing times.

Final procedures: heat treatment of d-UO_2 with high pO_2 and temperatures.
This incident demonstrated the risk of extended intervals at elevated temperature, so the system was redesigned during quarter 8 to allow the use of atmospheres with greater oxygen content (up to ~10^{-1} atm) [2]. Higher soak temperatures (>1530 °C) would result in shorter hold times (1-2 hours) to minimize potential equipment issues. This latest system iteration utilized a high temperature furnace (1700 °C rating) that was repaired and upgraded, and a redesigned gas system. The higher oxygen content and increased temperature capability resulted in greatly increased oxidation kinetics and facilitated growth of even larger grains than previous

procedures, without the risk of crossing a phase boundary into the adjacent two-phase region and damaging the sample (**Fig. 3C**, green lines). Various processing conditions were chosen (summarized in **Table 1** at the end of this section) to produce large-grained samples as efficiently as possible; samples with very large grains were indeed produced (**Fig. 4**) but the resulting mass losses (10-50%) due to evaporation from high UO_3 vapor pressure (**Fig. 5**, green lines) were deemed unsuitable for production of specimens. Efforts at this point shifted from heat treatment to sintering, as described next.

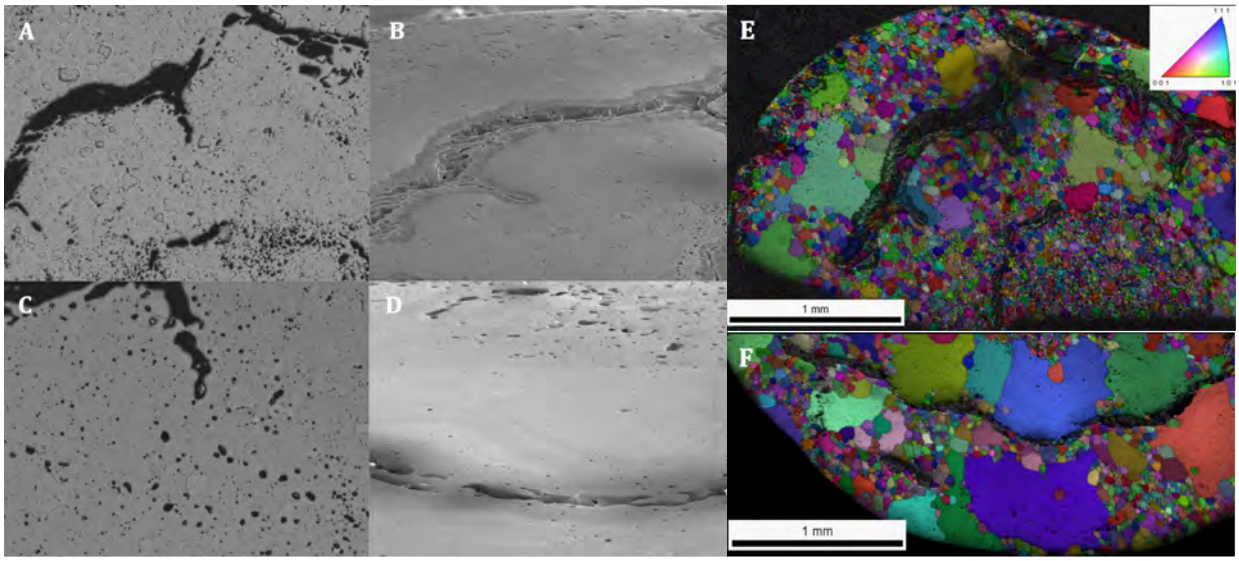

Fig. 4. Optical (**A**: 4x, **C**: 10x) and scanning electron (**B**, **D**) microscopy images of sample 12571-1 after heat treatment and surface polishing. Note the presence of large and contiguous voids across the surface of the sample, which likely contributed to sample breakage under thermal stresses. **E, F**) EBSD IPF maps overlaid on image quality (IQ) data for sample 12571-1 upper (**E**) and lower (**F**) halves after HT 8; area average grain size increased from ~9 µm to ~280 µm.

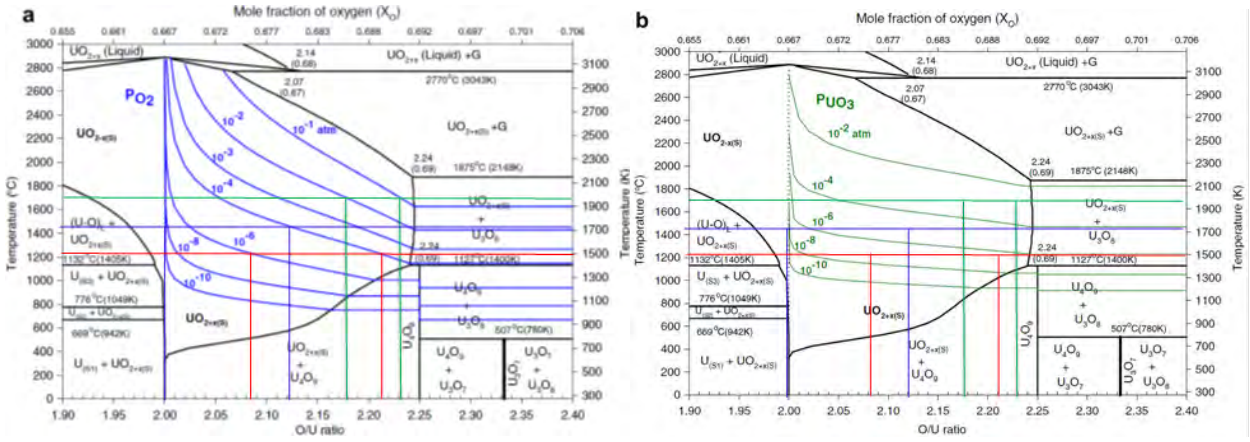

Fig. 5. **A**) Phase diagram of the U-O system [1] showing the conditions for experiments using revised procedure (v3.0, green). Previously reported procedures shown for comparison (v1.1, red, and v2.0, blue). **B**) Phase diagram of the U-O system overlaid with pUO_3 isobars [1] with processing conditions shown. HT 7 resulted in loss of 48% of initial mass due to evaporation; pUO_3 was found to be ~10^{-3} to ~10^{-2} atm, causing rapid evaporative losses.

Table 1. Summary of heat treatment procedures, with resulting grain sizes and mass loss.

Procedure	Sample	Temp (°C)	pO_2 (atm)	Time (h)	d_i (μm)	d_f (μm)	Mass loss (%)
1	38	1250 (1100)	$\sim 7x10^{-7}$	2.5	13	12	N/A
2	38	1250 (1100)	$\sim 1x10^{-4}$	2.5	12	12	N/A
3a	38	1200	$\sim 1x10^{-4}$	48	12	9.9	N/A
3b	38	1220	$\sim 5x10^{-5}$	48	9.9	13 (15)	N/A
4	38	1460	$1.0x10^{-4}$	76	15	25	N/A
5	38	1485	$1.0x10^{-4}$	192	25	24	N/A
6	15-115	1700	$1.0x10^{-4}$	5	15	19	7.87
7	15-115c	1700	$2.1x10^{-1}$	1	19	24	47.8
8	12571-1	1700	$2.1x10^{-1}$	0.5	9	280	48.0
9	12571-2	1600	$1.0x10^{-2}$	2	9	34	28.1
10	12571-2	1700	$2.1x10^{-1}$	1	34	150	45.0
11	15-112	1700	$2.1x10^{-1}$	1	30	39	9.33
12	15-112	1700	$2.1x10^{-1}$	5	39	50	51.5
13	12571-3	1700	$2.1x10^{-1}$	5	9	41	21.3

1.1.2. Pressing and Sintering of Powder Compacts

To fabricate an adequate supply of suitable specimens and meet the needs of project deliverables, arrangements were made with Areva of North America to procure high quality production UO_2 powder from each for the purposes of pellet fabrication. These powders were used to press green pellet compacts, ~6 mm in diameter and ~5 mm tall, which were then sintered under oxidative atmosphere to grow multi- and single-crystal samples based on [2]. Feedstock powders were used as-received to gather baseline data; later pellets were pressed with milled powder. Milling was performed using a SPEX planetary mill in an inert atmosphere within a secondary glove box commissioned for this use (**Fig. 6A**). Powder charges of 5-10 cm^3 were loaded into a zirconia milling vial along with 5 mm diameter zirconia milling media; to ensure a leak-proof seal, the lid of the vial was fitted with a corprene gasket primary seal, silicone 70 O-ring secondary seal, and a polyethylene film tertiary seal, secured by adhesive tape. Powders were milled for 30-60 minutes, then de-agglomerated through a 200-mesh sieve. Pellets were initially pressed in a servo-hydraulic load frame using a sealed and shielded isolation housing; the PI's lab later procured a specialized pellet press that could be installed in a glovebox, to minimize contamination, reduce the number of processing steps, and increase efficiency (**Fig. 6B/C**). An example pellet before and after oxidative sintering can be seen in **Fig. 7**.

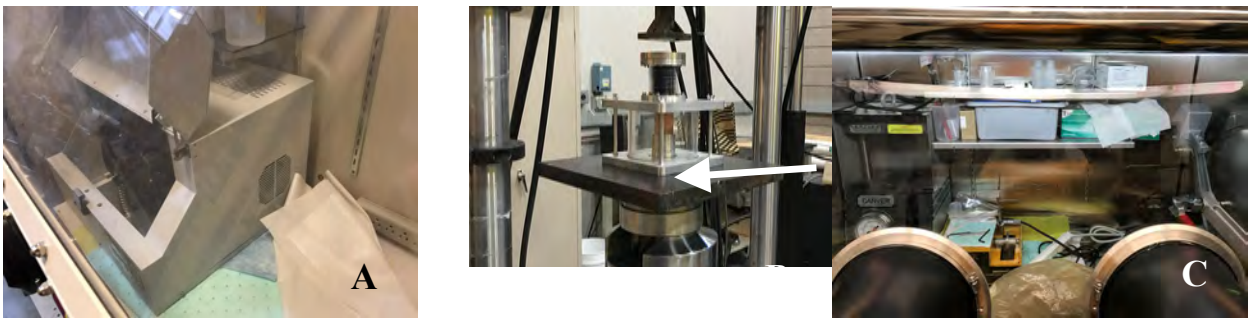

Fig. 6. Pellet pressing equipment: **A**) sealed, shielded housing with die installed, used for initial pressing procedures; **B**) lab pellet press (arrow) installed inside inert gas glove box, used for all subsequent procedures. **C**) SPEX planetary mill, installed in secondary inert-gas glove box.

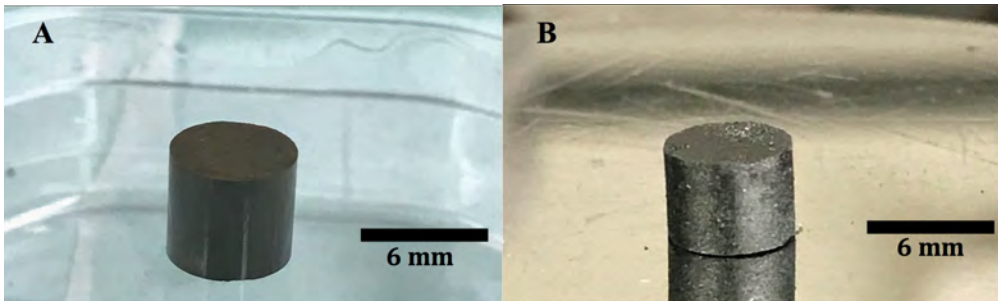

Fig. 7. UO_2 pellet before (**A**) and after (**B**) oxidative sintering.

Fig. 8 shows the processing furnace system in its final configuration; maximum throughput was one cycle per day, 1-3 pellets per cycle. The procedure used is based on [2]. Stoichiometric multi- and single-crystal samples were harvested and successfully tested (description in the next section), and hyper-stoichiometric samples (O/U ratio ~2.19) were also produced and tested. Pellets from initial procedures are shown in cross-section in **Fig. 9**, with a sample from the earlier heat treatment experiments on pre-sintered material included for comparison. Resulting grain sizes are on the order of ~1 mm, with various orientations and configurations available for use in testing procedures; an example of the sectioning process can be found in **Fig. 10**.

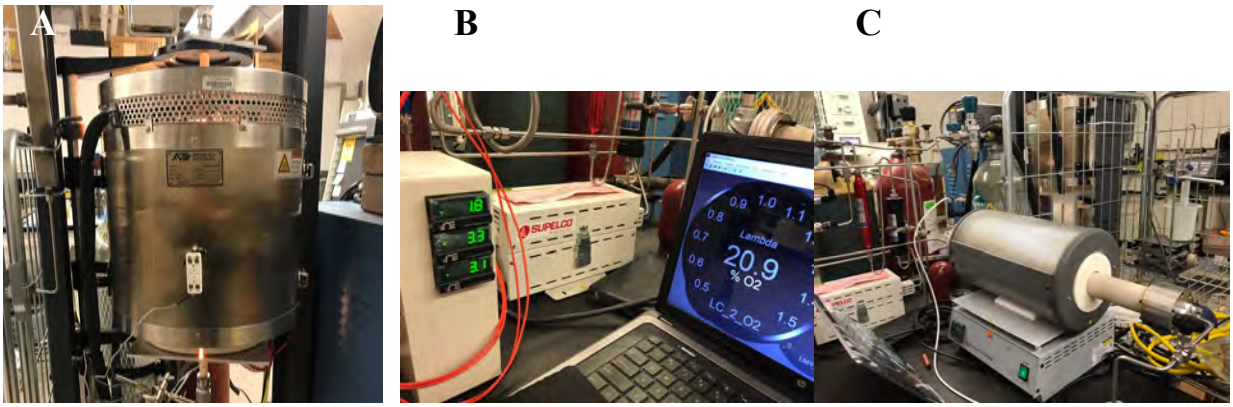

Fig. 8. Final configuration of elevated-temperature processing system, shown here during sample production: **A**) 1700 °C furnace. **B**) Process gas control/monitor setup (purifiers can be seen behind). **C**) Tanks containing certified mixtures, with precision metering valves and pressure transducers; also shown is the furnace containing a lab-grade precision oxygen measurement sensor (reads $pO_2 \geq 10^{-24}$ atm).

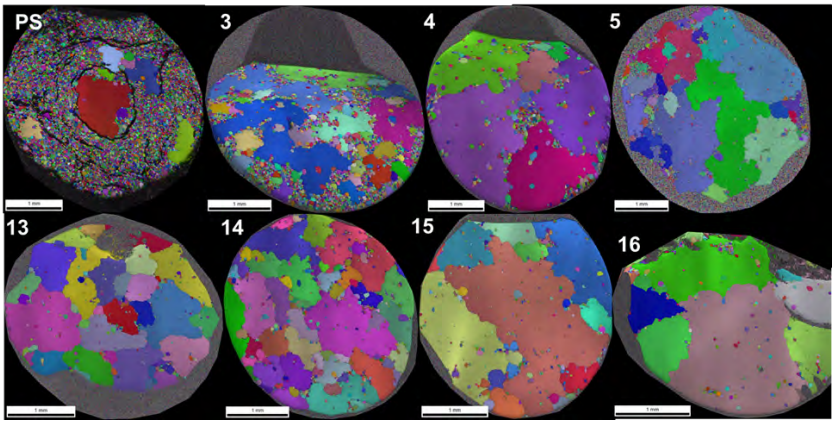

Fig. 9. Progression of sintering results for UO_2 samples pressed from feedstock powder (**3-16**); results from heat treatment of a pre-sintered sample (**PS**) also shown for comparison.

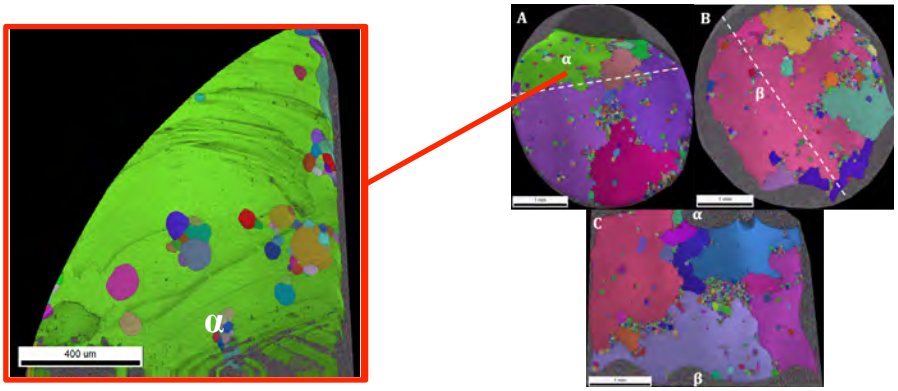

Fig. 10. Example sectioning procedure, where four single- and multi-crystal samples were harvested: **A**) top surface, **B**) bottom surface, and **C**) transverse cross-section. Dotted line indicates sectioning location; symbols denote orientation of cut surfaces. Inset: Top surface of single crystal sample 17-004-α-1, used in Creep Test (CT) 8.

1.1.3. Micro-scale Specimen Fabrication

A fundamental step required to achieve this project's objectives was mechanical testing of specimens at the microscale. This required the development of micromachining techniques to fabricate specimens such that they were contained mostly (or completely) inside a single grain. Techniques were developed for this purpose using Focused Ion Beam (FIB) to fabricate microcantilever beams that could be machined parallel to any crystal direction contained in the plane of the sample surface. This led to higher flexibility for probing anisotropic properties as compared to micro-pillars, which are limited to the direction normal to the sample surface. Through literature searches and evaluations of the difficulty (or ease) of fabrication, a geometry proposed by Di Maio and Roberts [5], shown in **Fig. 11**, was first adopted for the micro-cantilever beams to be used in this work (**Fig. 12**). This geometry has the advantage that it can be placed anywhere on the sample surface, which overcomes the slightly higher difficulty to fabricate it as compared to rectangular beams, which can only be placed at the edge of the sample.

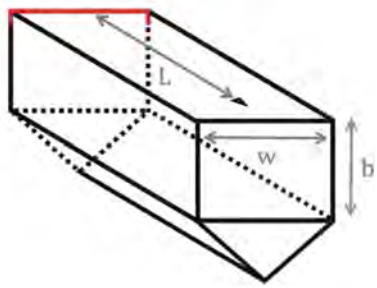

Fig. 11. The geometry from Di Maio and Roberts [5] for micro-cantilever beams.

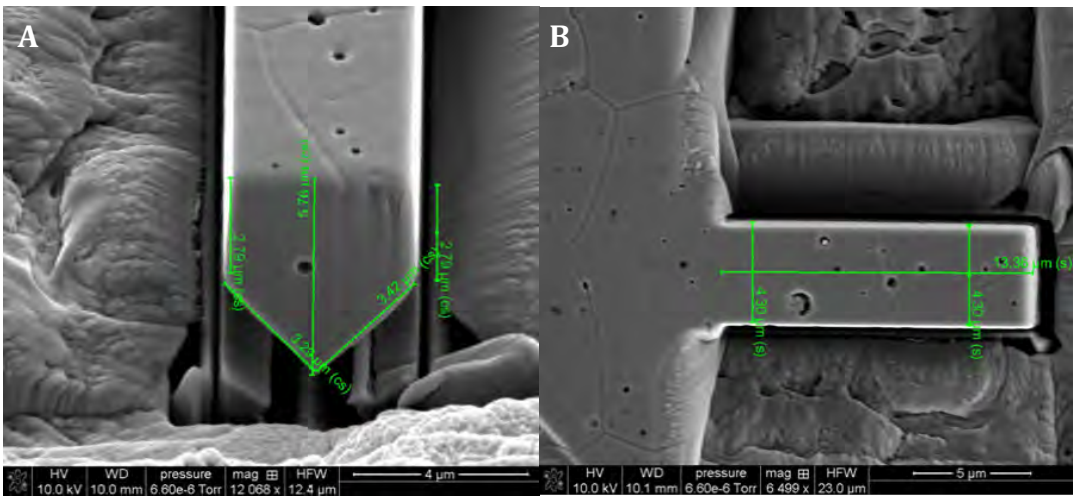

Fig. 12. Geometry of a finished micro-cantilever in UO_2 ready for testing. **A**) Cross-section, and **B**) plane view.

Beginning with the set of micro-cantilever beams manufactured during quarter 4, the length was increased by approximately 50% (15 µm to 22 µm) to reduce the uncertainty and error of the measurements, as well as the penetrations of indenter into the microcantilever, all of which can affect the results significantly when beams have a lowlength to height ratio (L/H); in [6] it was found that longer cantilevers produced more accurate values for E. This is particularly important since the stress is proportional to length, and the deflection is proportional to the length cubed. The increase in length also reduces the force needed to deflect and fracture the microcantilever, which in turn reduced the penetration of the indenter into the material. Using the stress versus displacement and E versus displacement curves a stress versus strain curve can be produced, as shown in **Fig. 13**.

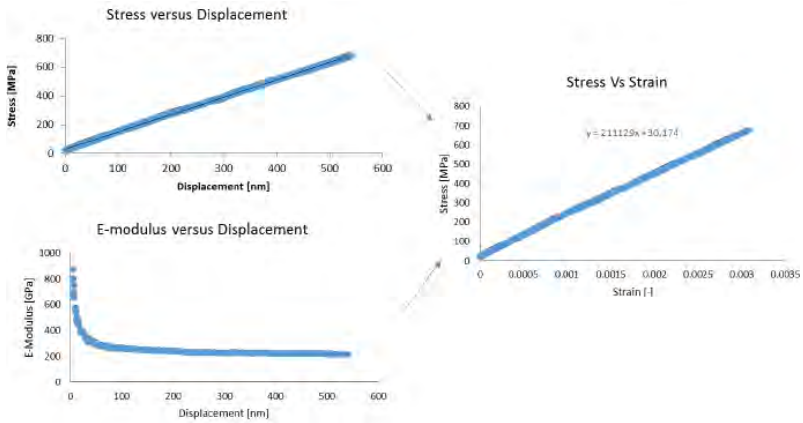

Fig. 13. Stress versus displacement, E versus displacement and stress versus strain plots for one of the tested micro-cantilever beams.

A linear fit can be made to the stress-strain curve and can be compared to the value of E calculated using equation 1, which assumes beam theory is accurate, which should be the case given the new length used for the beam, as per the results reported in [6]:

$$E = \frac{PL^3}{3\delta I} \tag{1}$$

Where P is load, L is the length from the loading point to the fracture surface, I is the moment of inertia and δ is the displacement of the indenter, which is assumed to be the same as the deflection of the micro-cantilever beam. The value calculated with the equation and the value from the linear fit to stress versus strain curve are essentially the same; this eliminated an important source of uncertainty as the project moved forward.

Other factors that might affect the local value of E for the material were also investigated. Initially, the microcantilever beams were manufactured near Vickers indents used as fiducials as to easily locate the micro-beams and the corresponding grains in EBSD scans. To evaluate whether the Vickers indents were affecting the properties of the material around the indent and possible the micro-beams, fields of nano-indents were performed next and far away from the Vickers indents (**Fig. 14**).

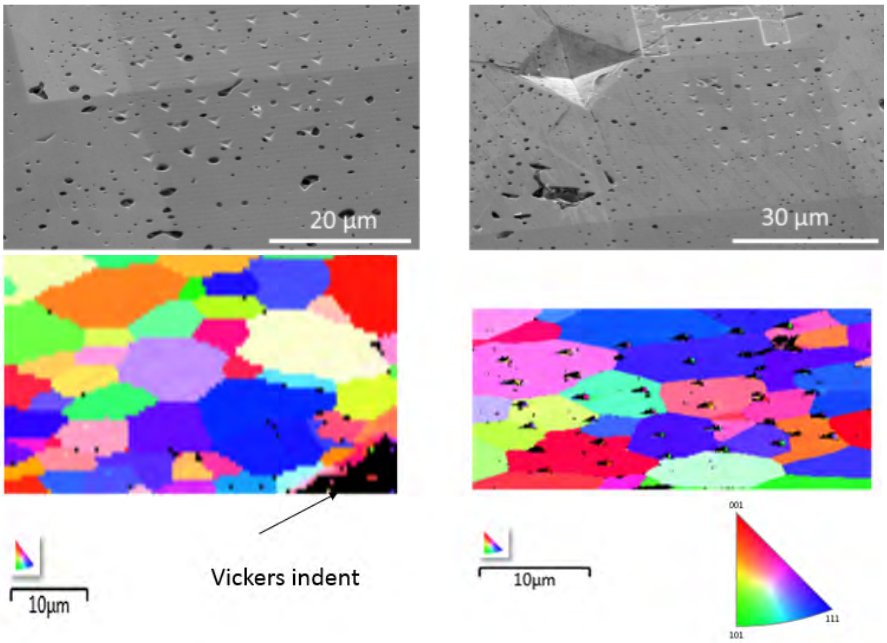

Fig. 14. Top: SEM images of nanoindentation fields far and near a Vickers indent. The H shape feature (right) was cut with the FIB to allow easy location of nanoindentation location in the SEM and the optical microscope used on the nanoindenter. Bottom: EBSD measurements before (left) and after (right) indentation.

It was found that the average hardness of indents next to the Vickers hardness was the same as the value far away from the indent. In addition, there was no statistically meaningful difference between the reduced modulus (E_r) values at the two locations obtained from the nanoindentation. The reduced modulus measured via nanoindentation, which is obtained from the unloading compliance, can be converted to the regular value of E using:

$$\frac{1}{E_r} = \frac{1-\nu_i^2}{E_i} + \frac{1-\nu_s^2}{E_s} \tag{2}$$

In equation (2) E_r is the reduced modulus, ν_i is Poisson's ratio for tip (.07), E_i is E for the indenter tip (1141 GPa), ν_s is Poisson's ratio for the sample (0.32 [7]), and E_s is E for the sample.

Examples of fabricated specimens with the higher values of L/H micro-machined along different crystallographic directions on a UO_2 substrate are shown in **Fig. 15**, including samples machined at the edge, where a rectangular cross-section could be used.

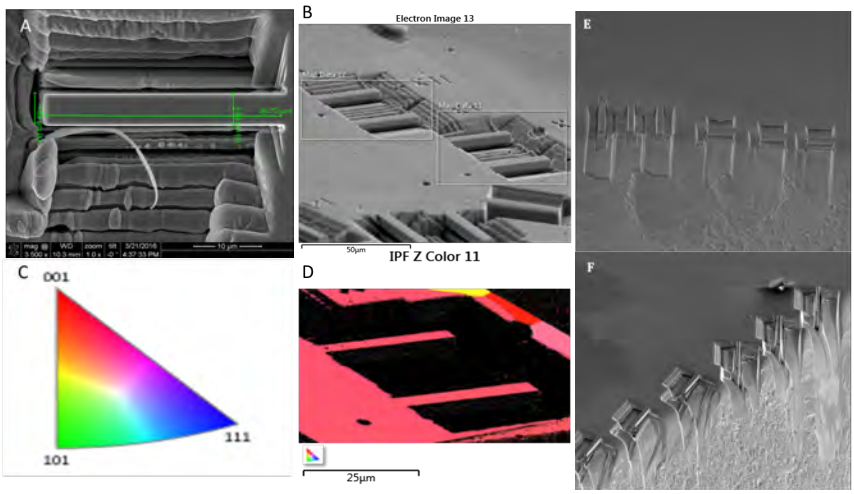

Fig. 15. **A**) A top down view of a microcantilever showing the length and width. **B**) An overview of the micro-cantilevers in the UO_2 showing one group of 4 micro-cantilevers. **C**) The inverse pole figure (IPF) coloring for the IPF map in image **D**. **D**) The IPF Z map of Map 11 in image B showing that both cantilevers are in the same grain. **E**) 6 micro-cantilevers with 3 parallel to edge and 3 perpendicular. **F**) SEM image showing 6 micro-cantilevers with 3 at 15° angle to edge and 3 at angle 45° to edge.

1.2. Mechanical Testing

Main Task 2 of this project requires mechanical testing to study thermo-mechanical response of UO_2 samples, at both the micro- and macro-scale. The purpose of using different length scales was two-fold: to investigate the effects, if any, of specimen size on mechanical properties of UO_2, and collect valuable data with which to calibrate and validate computational models as required in Main Task 3. To that end, procedures were developed to: 1) test UO_2 samples at the micro- and macro-scale, under atmospheres with controlled oxygen partial pressures, using variables of stress, temperature, and stoichiometry; 2) perform surface characterization of identical areas before and after each experiment, with no further post-procedure surface preparation needed; 3) collect data of sufficient quality from each procedure. Once suitable samples were provided by efforts of Main Task 1, grains were then carefully selected based on their crystallographic orientations to perform ex-situ micro-mechanical tests with samples machined via Focused Ion Beam (FIB), with emphasis on micro-cantilever bending. These experiments were performed under controlled atmospheres, to insure stoichiometry control, at temperatures up to 700 °C, allowing measurement of properties involving elastic (effective Young's modulus), plastic (critical resolved shear stresses) and creep (creep strain rates) behavior. Conventional compression experiments were performed simultaneously to compare with the ex-situ measurements and study potential size effects; results are summarized in the following section.

1.2.1. Macroscale Creep Experiments

Macro-scale testing was comprised of instrumented uniaxial compression creep experiments performed at elevated temperature, under both reducing and oxidative atmospheres, to study the effect of load, temperature, and stoichiometry on the intra-granular thermo-mechanical response

in UO_2 as required by Main Task 2. Temperatures were chosen in the range of 900-1200 °C to more closely simulate reactor operating conditions, with stresses ranging from 20-110 MPa. Testing was conducted using an Instron load frame, first under servo-hydraulic control, then later utilizing a dead-weight loading system specifically fabricated for the purpose of constant-stress testing (**Fig. 16**); use of dead weight ensured consistent sample loading regardless of environmental conditions or the presence of electrical noise affecting sensor readings. Samples were loaded using ceramic platens attached to the end of alumina rods and the loading surfaces were lubricated with boron nitride to reduce friction (and barreling) during the compression tests. The experiments were performed at 1200 °C under Ar-4%H_2 atmosphere (for stoichiometric testing) and UHP Ar (for hyper-stoichiometric testing) to keep the oxygen content consistent. Samples with various microstructures were loaded under the above conditions while data was collected from a load cell, extensometer, precision micrometer, oxygen probes, and thermocouples measuring load, strain, displacement, pO_2, and temperature, respectively. Polycrystalline samples were tested initially, the results of which served as a baseline validation of data precision through comparison with results for similar tests published in literature. EBSD orientation data was collected from identical areas of polished surfaces parallel to the loading direction, i.e., not in contact with the loading platens, using OIM software before and after each procedure, to facilitate a direct comparison of surface features and characterize microstructural changes due to elevated-temperature plastic deformation. Strain data collected was then compared to measurements taken using a precision micrometer (to verify changes in height and overall strain) and correlated with OIM data to find Critical Resolved Shear Stresses (CRSSs) and shear strains for each crystal orientation. Axial strain vs. time data is shown in **Fig. 17**, and a summary of measurements and testing data is shown in **Table 2**.

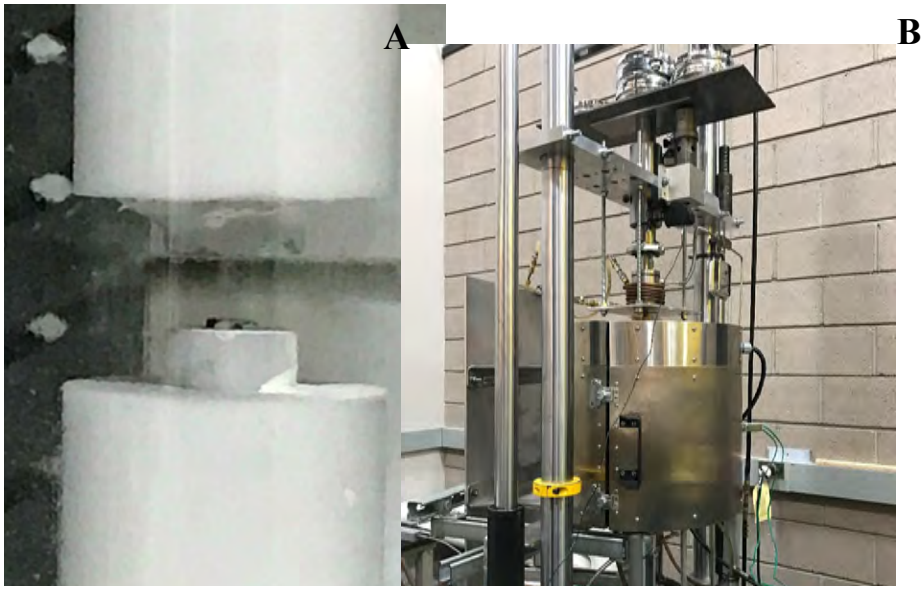

Fig. 16. **A**) Loading rods with polished platens, shown with sample loaded. **B**) High-temperature testing apparatus, sealed and purged prior to testing.

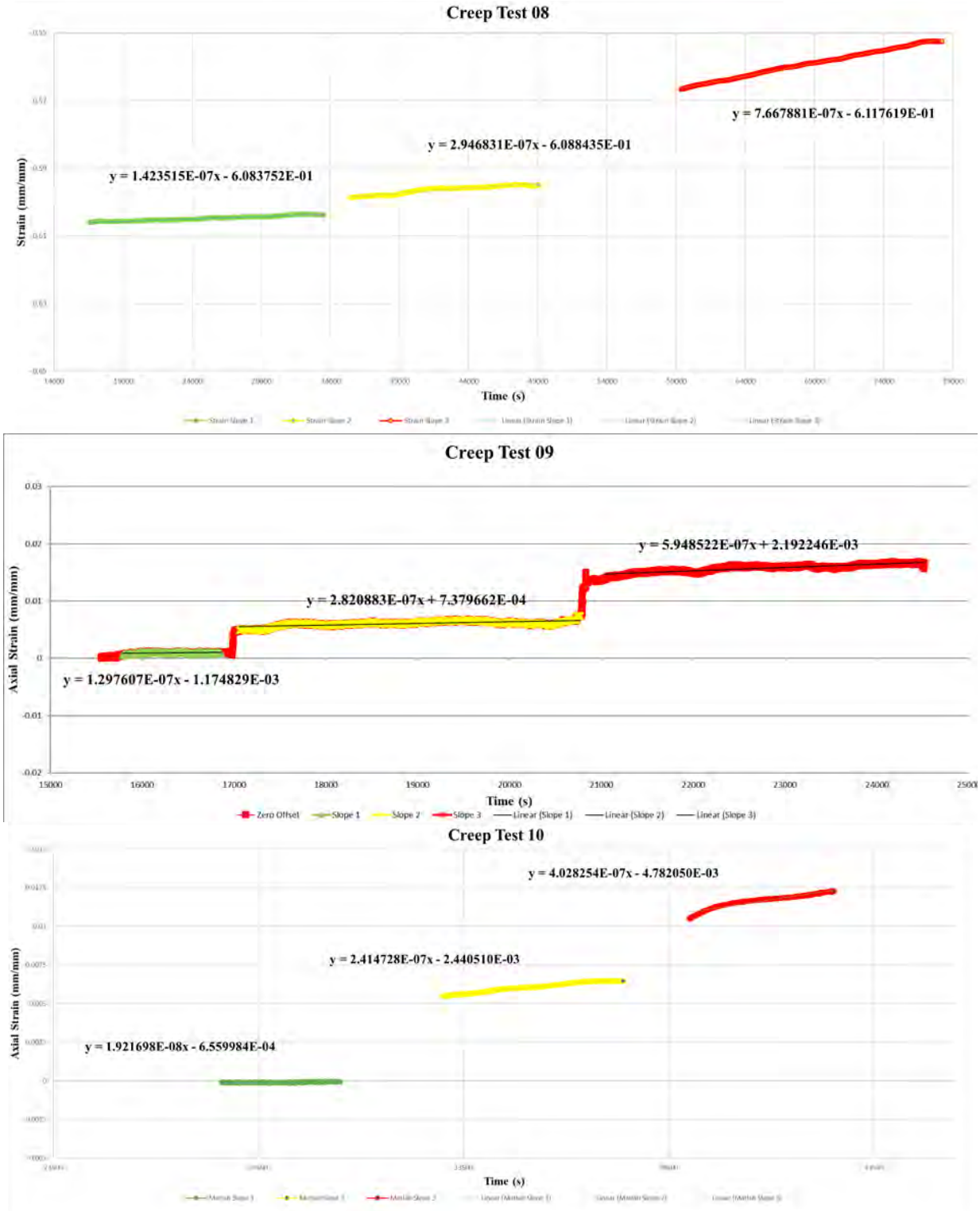

Fig. 17. Strain vs. time for single crystal (CT8), bi-crystal (CT10) and hyper-stoichiometric (CT11) samples; linear fits indicate average steady-state strain rate.

Table 2. Summary of Uniaxial Compression Creep Test Procedures

Test	Temp (K)	Stress (MPa)	Time (h)	$\dot{\varepsilon}_{ave}$ (s^{-1})	ε_t (%)	Δh (mm)	Sample
1	1173	25.1	6.0	-3.46×10^{-8}	-0.60	-0.02	10-218
2	1173	23.4	6.0	-5.74×10^{-8}	-0.98	-0.05	10-213
4	1473	26.6	4.0	N/A	-0.02	-0.01	10-213
5	1473	28.7	6.0	-8.96×10^{-8}	-1.06	-0.05	10-213
6	1473	181	6.0	-6.43×10^{-6}	-9.11	-0.06	12571-1-α
7	1473	68.0	6.0	-8.22×10^{-7}	-0.82	-0.01	12571-1-β
8	1473	63.0 82.6 110	5.5 4.0 8.0	-1.42×10^{-7} -3.01×10^{-7} -7.67×10^{-7}	-10.76	-0.26	17-004-α-1
9	1473	31.2 39.9 50.3	1.0 1.0 1.0	-1.30×10^{-7} -2.82×10^{-7} -5.95×10^{-7}	-1.79	-0.06	17-004-β-1
10	1473	30.0 41.3 49.6	1.0 1.0 1.0	N/A -2.41×10^{-7} -4.04×10^{-7}	-0.47	-0.015	17-004-β-2
11	1473	30.0 39.1 50.1	1.0 1.0 1.0	-2.72×10^{-6} -5.60×10^{-6} -1.13×10^{-5}	-15.12	-0.53	18-024-α

In addition to EBSD scans, dislocation trace imaging and analysis of the deformed surface of the single crystal sample was performed using ECCI. A technique was developed for precise positioning of the sample surface relative to the incident beam and used for the single- and multi-crystalline samples; Kikuchi backscatter diffraction patterns generated via the rocking-beam function of the Tescan Vega-II column in conjunction with a solid-state backscatter detector (BSD) facilitated real-time monitoring of the sample position as outlined in [8]. The single-crystal sample tested in procedure 8 was purposely deformed to the extent that shear strain produced surface topography (slip traces) that could be detected using an optical microscope, to facilitate further examination using optical profilometry for quantitative information on local shear strain (**Figs. 18-19**). Schmid factors and resolved shear stresses for the individual grains in each sample are shown in **Table 3**. Strain rates for macro-scale polycrystalline samples used for proof-of-principle tests were in good agreement with literature, while results for single- and multi-crystal specimens suggested a climb-assisted dislocation glide mechanism in the (001)[110] slip system.

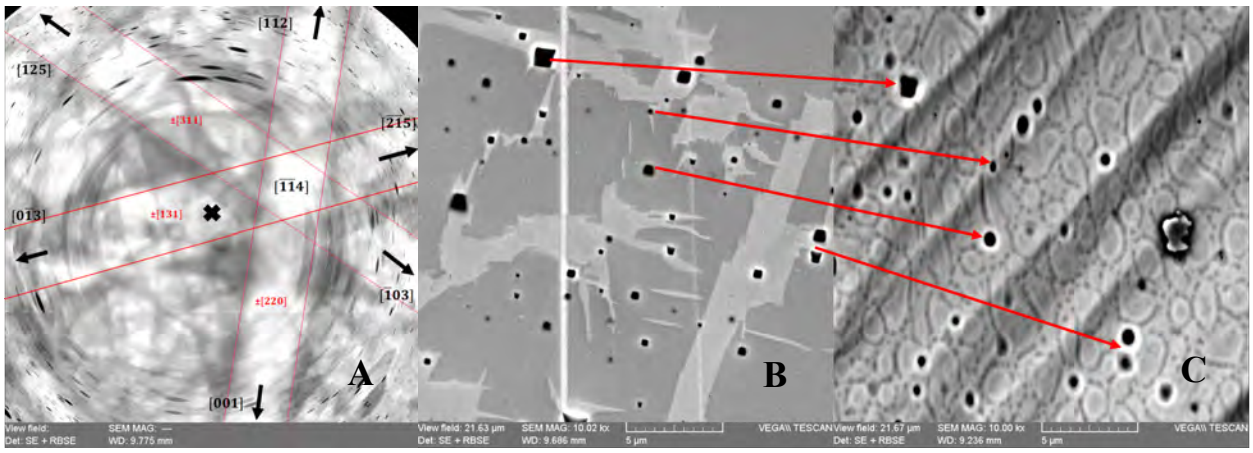

Fig. 18. **A**) Rocking-beam electron backscatter diffraction pattern, with nearest zone axis and neighbor zone axis labeled in black; Kikuchi bands are labeled in red. **B**) BSD image of sample surface, before deformation. **C**) Identical area, after deformation; note presence of dislocation cell structure and surface topography. Red arrows indicate pores used as fiducials for positioning.

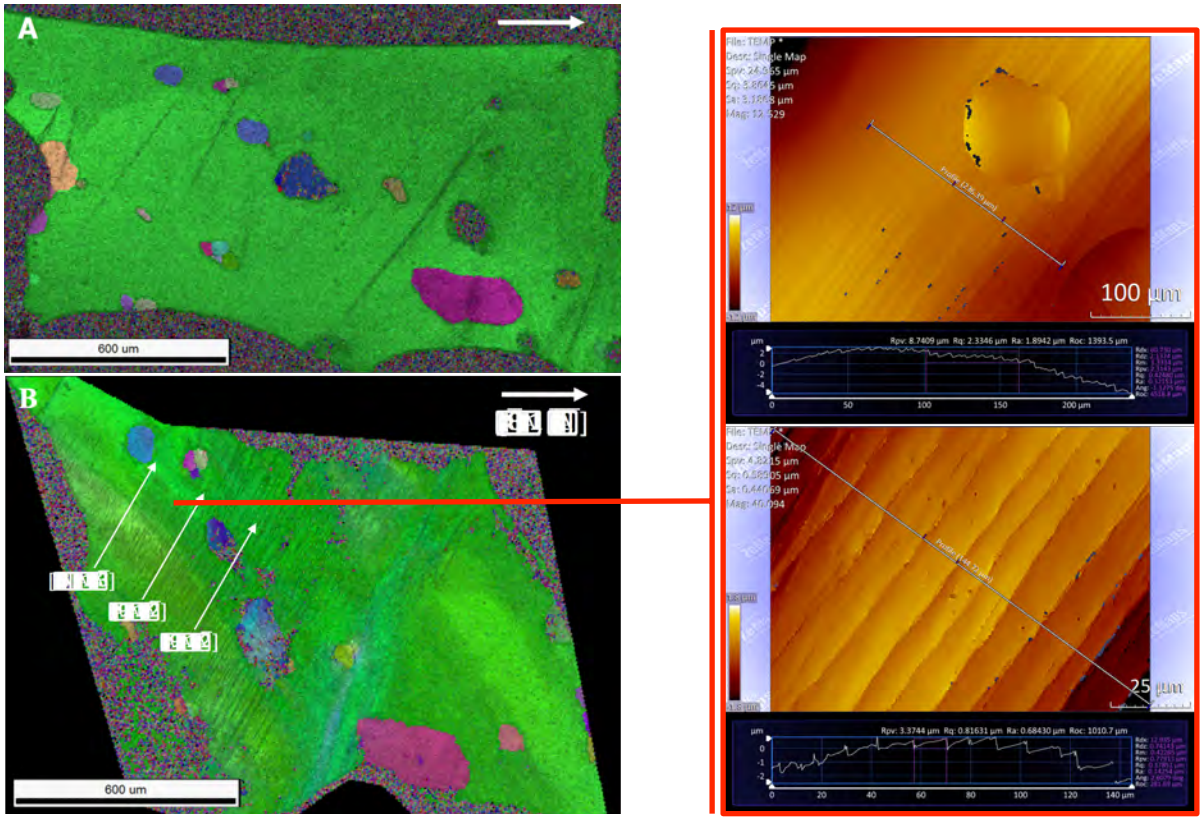

Fig. 19. EBSD inverse pole figure map, before (**A**) and after (**B**) deformation; the arrow indicates the loading direction. Note the overall distortion present in (**B**) has a component of displacement normal to the loading direction and coincides to the diagonal striations on the surface. These are slip plane traces, close to (100) type; arrows are labelled using indices from OIM analysis software (measurements made with respect to the loading direction, which itself is close to [101]). **Inset:** Optical profilometry measurements of resulting surface texture, 12.5x (top) and 40x (bottom).

1.1.1.1. Stress Exponent Analysis

Table 3 details the structures and orientations of the single- and multi-crystal specimens used in test procedures 8-10; data collected from these tests were used to calibrate and validate the crystal plasticity model (ref. section 2.1.1). Each specimen featured a columnar structure of 1-3 large grains, which dominated the microstructure and subsequently the thermo-mechanical response. The orientations listed are with respect to the loading axis, given in integer (hkl)[uvw] indices, and the shear stress values shown were calculated using the Schmid Law for single-crystal slip.

Table 3. Summary of Sub-Grain Deformation Analysis

Test	Structure	Orientation	*n*	SF	τ_c (MPa)
8	Single Crystal	$(\bar{5}\ 7\ 0)[7\ 5\ 37]$	3.03	0.34	21.4 28.1 37.4
9	Bi-crystal	$(7\ 10\ 18)[6\ 3\ \bar{4}]$ $(5\ \bar{7}\ 26)[25\ \overline{23}\ \overline{11}]$	3.16	0.45 0.30	14.04 17.96 22.64 9.36 11.97 15.09
10	Bamboo	$(7\ 10\ 18)[6\ 3\ \bar{4}]$ $(\bar{5}\ 7\ 0)[7\ 5\ 37]$ $(\bar{8}\ 1\ 22)[18\ \overline{10}\ 7]$	3.01	0.45 0.48 0.26	13.5 18.59 22.32 14.4 19.8 23.8 7.80 10.7 12.9

For these procedures the specimens were subjected to three different loads (stress step testing), with each loading step being held until the sample reached the steady-state creep regime (Stage II Creep), and sufficient data recorded to calculate a statistically-relevant linear fit from which the stress exponent *n* could be determined (**Fig. 20**). The results for tests 8-10, performed on stoichiometric samples, are in agreement with data from experiments on single crystals found in early literature [9].

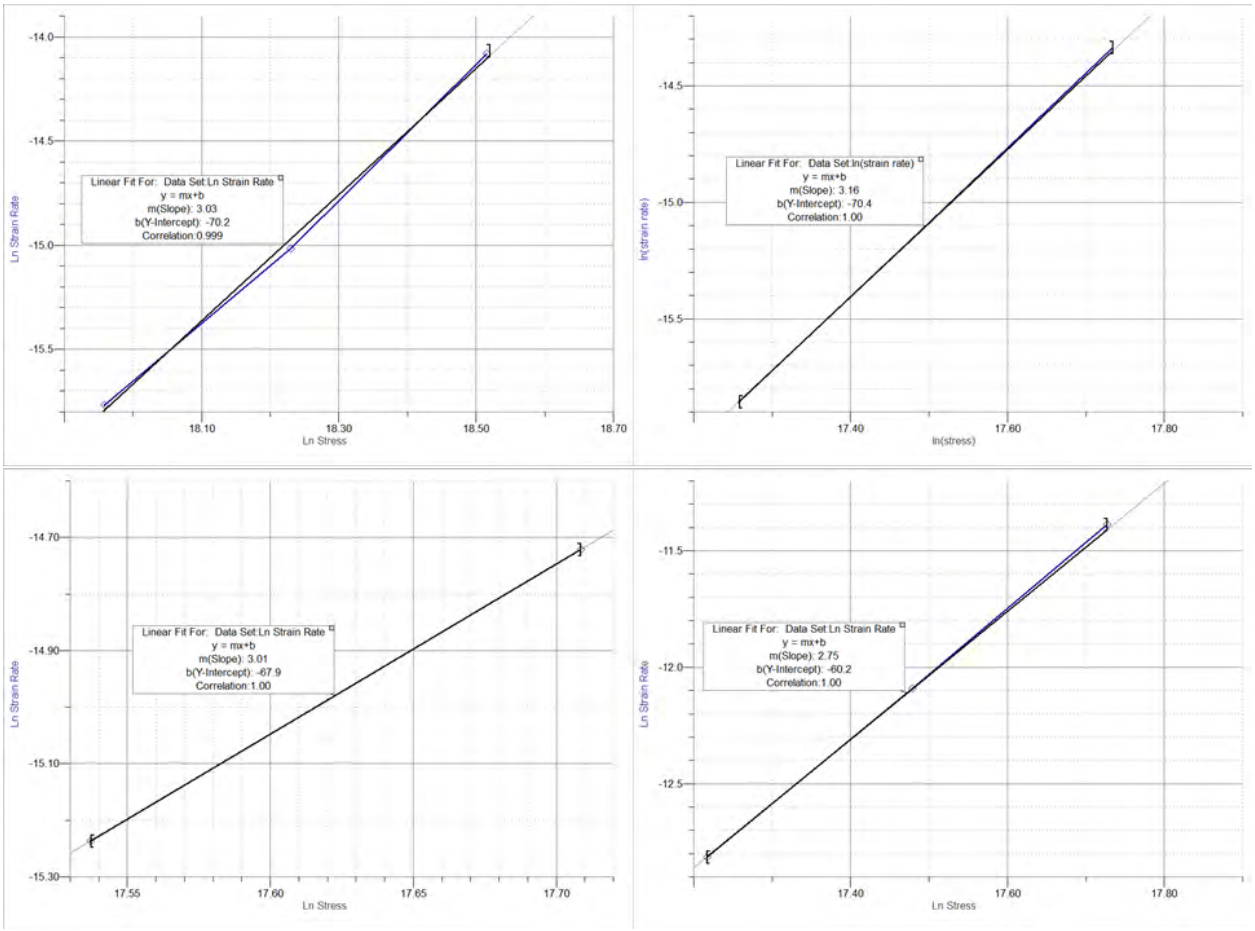

Fig. 20. Linear fits of log/log plots from each procedure; the slope gives the stress exponent *n* for each sample.

To ascertain the effects, if any, of stoichiometry on the thermo-mechanical response of UO_2, the experiment was repeated using a hyper-stoichiometric specimen, $UO_{2.19}$. The procedure used to synthesize hyper-stoichiometric samples was identical to that which produced UO_2 pellets, with the exception of gettered/trapped UHP argon being used to reduce the sample instead of argon/hydrogen; the O/M ratio was verified per ASTM C1430-07 [10]. Conditions (stress, time, temperature, etc.) for this procedure were identical to those of tests 9 and 10 to facilitate a direct comparison; a plot of axial strain vs. time is shown in **Fig. 21**. It was found that the $UO_{2.19}$ pellet had only a slightly lower stress exponent (2.75 vs. 3.01-3.16, **Figs. 17, 21**) but with strain rates (10^{-6} vs. 10^{-7}, **Fig. 20**) and overall deformation (15% vs. 0.47-1.79%, **Table 2**) greater by an order of magnitude, suggesting the creep regime for UO_{2+x} is the same as that of UO_2 but with a significantly reduced activation energy; further testing will be needed to validate this hypothesis.

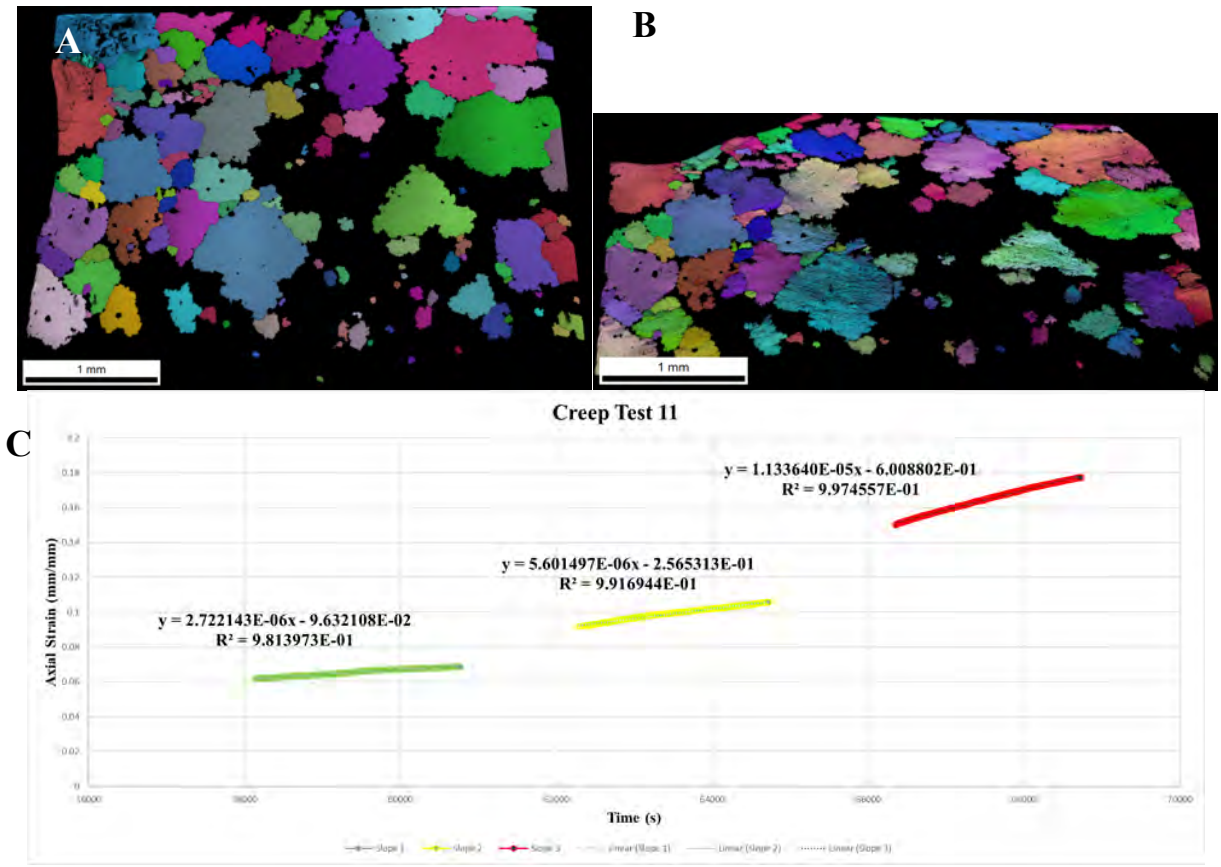

Fig. 21. IPF maps of UO_{2+x} specimen, before (**A**) and after (**B**) testing. **C**) Axial strain vs time, procedure 11 (UO_{2+x}). Note the significantly higher strain rates and extent of deformation as compared to UO_2.

1.2.2. Microscale Creep Experiments

The study of thermo-mechanical behavior in depleted uranium dioxide (d-UO_2) resulted in the successful completion of micro-mechanical testing of pre-strained samples. Macroscale compression creep testing at 1200 °C was employed to induce an initial strain in the sample of ~9%, with microstructural characterization before the tests using SEM imaging in conjunction with EBSD; this initial work was performed in the PI's lab at Arizona State University. The sample was then transferred to UC Berkeley, where nanoindentation experiments were performed in a controlled atmosphere at temperatures ranging from 25 °C to 700 °C to characterize the mechanical response of the pre-strained specimens at the microscale.

The sample was characterized before the creep procedure, using secondary-electron SEM imaging in conjunction with EBSD scans to verify the presence of large grains. Once the sample was suitably deformed, microscale mechanical testing was performed at UC Berkeley via elevated-temperature nanoindentation experiments in a controlled atmosphere. Indentation and indentation creep tests were completed successfully at temperatures of 25 °C, 100 °C, 300 °C, and 500 °C; a test at 700 °C was attempted, but ultimately proved unsuccessful due to contamination of the tip. Indents were load-controlled and load-terminated, with 20-second loading and 10-second unloading ramps; dwell times were 20-45 seconds (temperature dependent) for regular indentation and 300 seconds for indentation creep; testing was done on both the pre-strained sample and an un-strained sample for comparison.

Results of microscale indentation testing are given below. Plots of hardness and reduced modulus vs. temperature for indentation and indentation creep procedures are found in **Fig. 22**.

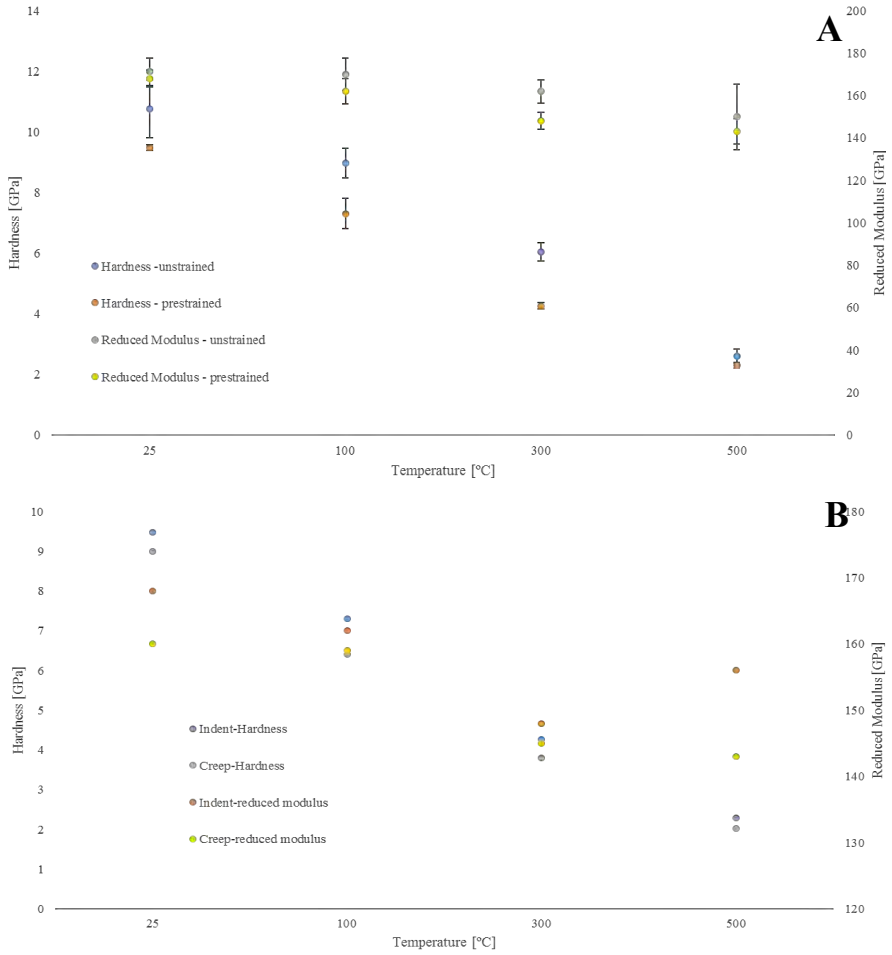

Fig. 22. A) Comparison of hardness and reduced modulus vs. temperature for indentation tests of the pre-strained sample and sample without pre-strain. **B**) Hardness and reduced modulus vs. temperature for indentation and indentation creep of sample with pre-strain.

Hardness values from indentation and indentation creep for both samples exhibit similar downward trends, which is expected with increasing temperature. Both the hardness and reduced modulus were lower in the pre-strained sample compared to the sample without pre-strain; the reduction in hardness was largest at temperatures lower than 500 °C, while the drop in reduced modulus was most obvious at the two intermediate temperatures. Lower values suggest an energetically-favorable microstructural change, such as the addition of dislocations introduced by the macroscale deformation, may have taken place; testing of additional specimens would be needed to further evaluate intrinsic material scatter and ensure statistical validation of results. **Fig. 22A** shows that, although hardness values for the pre-strained sample are lower than those of the sample without pre-strain, the difference between the behaviors at 25 °C and 500 °C is quite close to or within the error bars, indicating the need for repeat testing on additional samples at these temperatures to collect additional data from which to draw conclusions on the efficacy of pre-straining ceramic samples to facilitate low-temperature plasticity. The deviation in hardness is certainly larger than the error bars at 100 °C and 300 °C, suggesting that the benefits of pre-

strain are limited to a narrow temperature range. The changes in reduced modulus are on the same order of the error bars, so they cannot be considered statistically meaningful at this time.

Fig. 22B shows plots of the hardness and reduced modulus for indentation and indentation creep testing of the pre-strained sample only; the hardness from both tests follows the expected trend seen above in **Fig. 22A**, while the reduced modulus values seem to deviate at the highest tested temperature. This could be due to environmental factors, such as tip contamination. **Figs. 22-23** show the load vs. displacement curves from the indentation creep tests at each temperature; the upper plot of each figure is for the sample without pre-strain, while the lower plot gives data from the sample with pre-strain. In each case, additional deformation due to creep is evident during the dwell at maximum load (shown here as gaps opening between the loading and unloading curves) suggesting the pre-strain induced in the sample may have allowed for increased plasticity during the microscale tests.

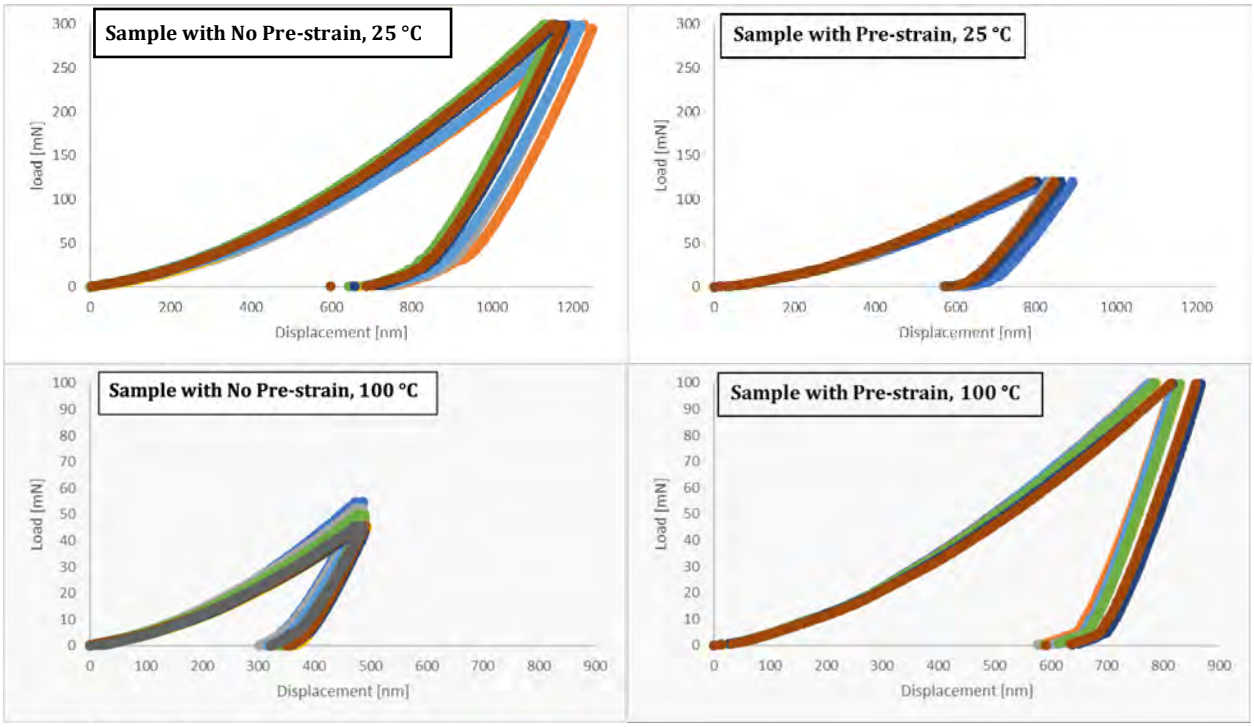

Fig. 23. Load vs. displacement for indentation creep tests at 25 °C (top) and 100 °C (bottom), with pre-strained samples vs. sample with no pre-strain.

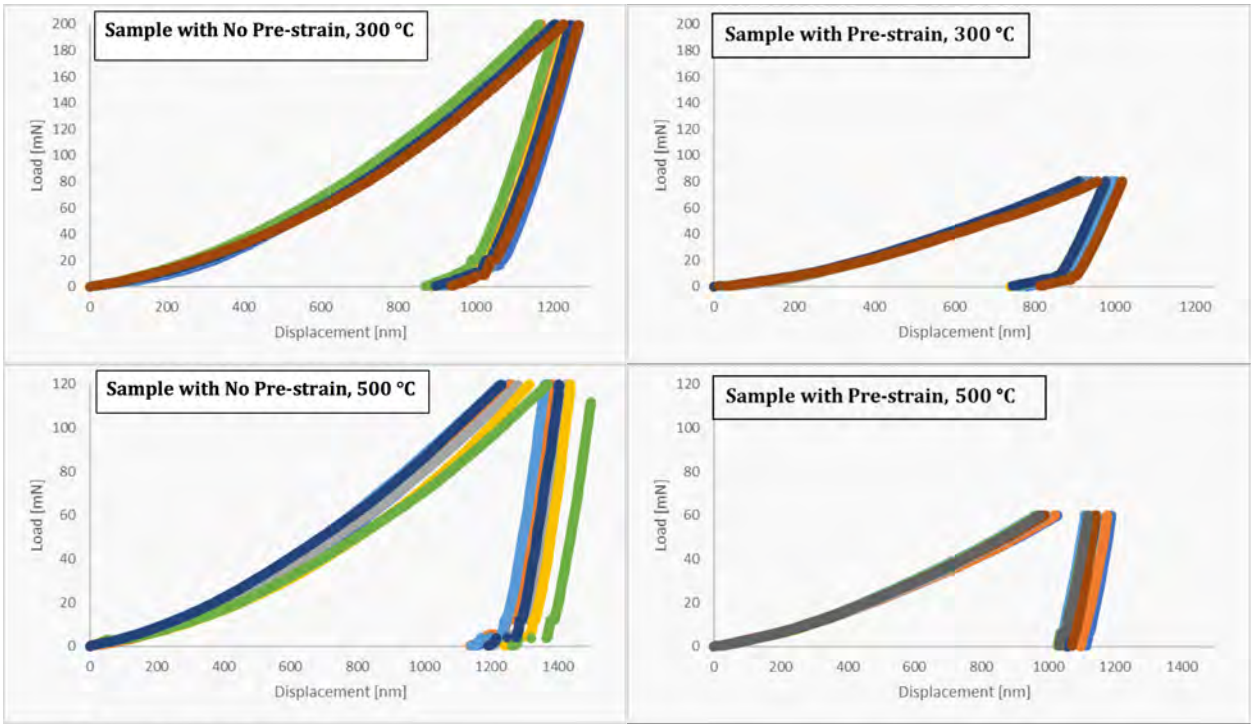

Fig. 24. Load vs. displacement for indentation creep tests at 300 °C (top) and 500 °C (bottom), with pre-strained samples vs. sample with no pre-strain.

It has been postulated that the high activation energy for dislocation nucleation in UO_2 at low temperatures is one of the critical factors for the lack of plastic deformation at those temperatures [11]; increasing the number of pre-existing dislocations should therefore facilitate a decrease in the effective activation energy for plasticity. The work reported here served to test this theory by deforming a specimen of d-UO_2 via macroscale compression creep testing at elevated temperature, then performing microscale creep testing at low temperatures of the pre-strained sample, alongside a sample without pre-strain for comparison. The results of this experiment suggest that the presence of strain induced at high temperature did have a measurable effect on the thermomechanical response of the material at lower temperatures, thus suggesting that this a possible method for inducing low-temperature plasticity, in agreement with results presented by Keller et al. [11, 12].

2. Computational Modeling

The study of thermo-mechanical behavior in depleted uranium dioxide (d-UO_2) resulted in the successful formulation, calibration, and validation of a crystal plasticity constitutive model to describe 1) the creep deformation of UO_2 at the sub-grain length scale (single crystal level) at intermediate temperatures, and 2) elasto-plastic deformation of microcantilever beams at moderate temperatures.

Macro-scale testing of UO_2 samples with large grains was performed at 1200 °C using a modified load frame at ASU capable of applying dead-weight loads to ensure constant stress conditions, while displacement of the sample produced by the applied load was measured with high precision micrometers to obtain strains. Stress steps were used during testing and the strains were monitored to measured creep strain rates under steady state for each level of stress used, so that stress exponents could be obtained. The results of the mechanical testing, along with sample

geometry and crystal orientation of the grains in the samples, as well as post-test sample characterization were used to formulate a viscoplastic model to account for steady state (stage II) creep behavior, along with basic assumptions from crystal plasticity and kinematic constraints due to testing fixtures.

Testing of microcantilever beams at temperatures ranging from 25 to 570 °C was performed at UC Berkeley in-situ with a scanning electron microscope with a special attachment to apply load and measure displacement while the samples was at temperature. The load-displacement curves obtained showed linear behavior before fracture for all temperatures attempted except 570 °C, where clear deviations from non-linearity were observed before fracture. These deviations were consistently observed for all samples tested for a given orientation. A viscoplastic model was used to account for the presence of inelastic strain, along with basic assumptions from crystal plasticity and beam theory. Both models were kept as simple as possible; the formulations and assumptions used are outlined below.

2.1. Collection of Experimental Data

2.1.1. Macroscale Testing Data

Samples were prepared from natural uranium oxide powder of production-quality provided by Areva. The powder was pressed in a die to a pressure of 100 MPa no produce green pellets with no sintering aids, lubricants, or any other additives. The green pellets were then heated up to 1700 °C under ultra-high purity argon atmosphere (~1 ppm O_2). The atmosphere was then changed to 79% Argon, 21% O_2 and the temperature was held at 1700 °C for 2 hours to sinter the pellets under oxidative conditions [2] that are known to increase grain growth kinetics in UO_2 [1]. Samples were then cooled down under Ar-4%H_2 atmosphere to reduce the samples back to stoichiometric UO_2. The resulting pellets were removed from the furnace and their top and bottom surfaces were ground and polished to analytical quality and were examined using EBSD to characterize their microstructures, with emphasis on grain size. Once maps of the grains on the top and bottom surfaces were obtained, specimens in the form of prismatic cylinders were obtained from the pellets, by sectioning them using a slow diamond saw. These samples were harvested such that the number of grains in each one of them was minimized, trying to get either single crystals or bi-crystals with a bamboo structure, i.e., two grains, one on top of the other, along the axis of the cylinder.

Once samples were sectioned, their lateral surfaces were also polished and characterized using EBSD to collect information from before the tests. The sections were then tested under conditions as outlined above (section 1.2.1, procedures 8-10) while the strain was monitored to make sure that the samples reached steady state before applying the next set of weights, so that stress exponents could be obtained from these step tests [13]. Samples were loaded using ceramic platens attached to the end of alumina rods and the loading surfaces were lubricated with boron nitride to reduce friction (and barreling) during the compression tests. The experiments were performed at 1200 °C under Ar-4%H_2 atmosphere to keep the stoichiometry of the samples. Once the last set of weights was applied and the strain reached steady state, the specimens were cooled down to room temperature still under Ar-4%H_2 atmosphere. Then the sample was removed to characterize the lateral surfaces using optical microscopy and EBSD to obtain information on slip traces and lattice rotations produced by the deformation process. In addition, ECCI was used to characterize the dislocation structure produced during the test. Microstructures of samples harvested from large grained pellets are shown in **Fig. 25**.

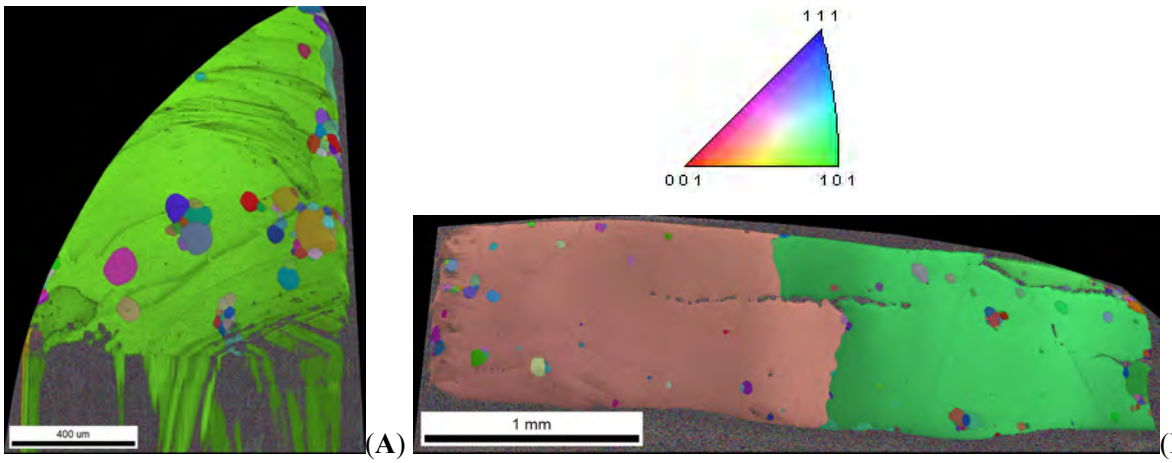

(A) **(B)**

Fig. 25. Examples of UO_2 specimen microstructures. **A**) Dominant single grain harvested from a large grained sample. **B**) Bi-crystal sample with a bamboo structure for a horizontal loading axis. The colors correspond to crystal orientations parallel to out-of-plane directions as per the standard triangle legend in the inset.

Mechanical testing within the high stress range was performed in the sample with a dominant single grain (**Fig. 25A**), and the bi-crystal sample with the bamboo microstructure was used for the low stress range. The bi-crystal sample experienced a total permanent strain of about 1.8%. The resulting strain versus time plots for the low stress case is shown in **Fig. 26**.

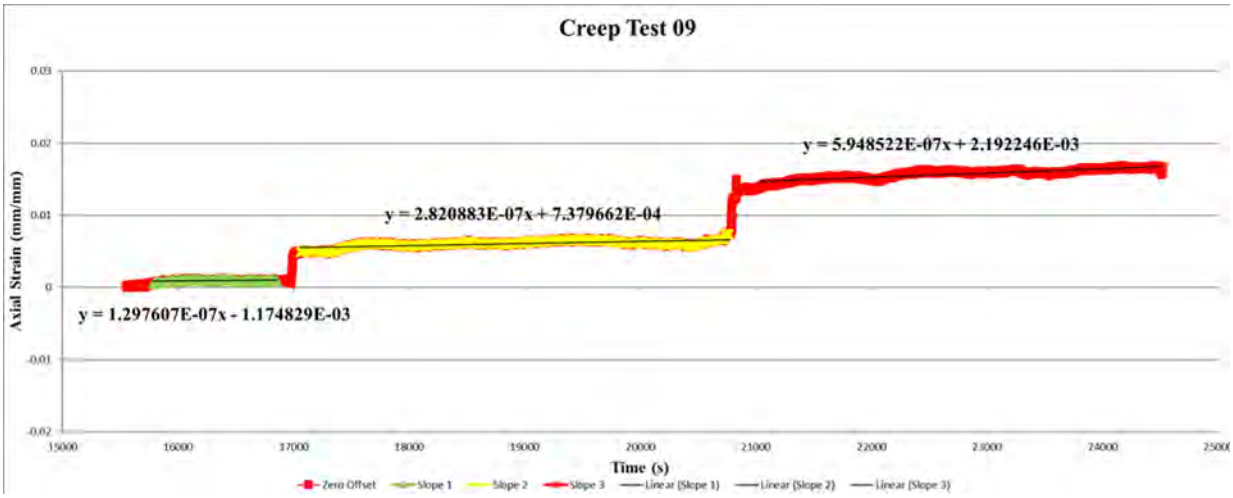

Fig. 26. Strain-time curve for a bi-crystal sample with a bamboo structure. Linear fits are shown for each steady state region. The stresses corresponding to each region are: 31.2 MPa, 39.9 MPa, and 50.3 MPa. The test lasted 3 hours. The strain axis has not been corrected for thermal expansion and initial offset of the displacement measurement.

The data from this test was analyzed to extract a stress exponent. In this case, data were plotted in log-log axes, which revealed a linear behavior in logarithmic axes, which implies that a power-law behavior can be assumed. The coefficient and exponent of this power law were obtained using least squares. Results are shown in **Fig. 27**.

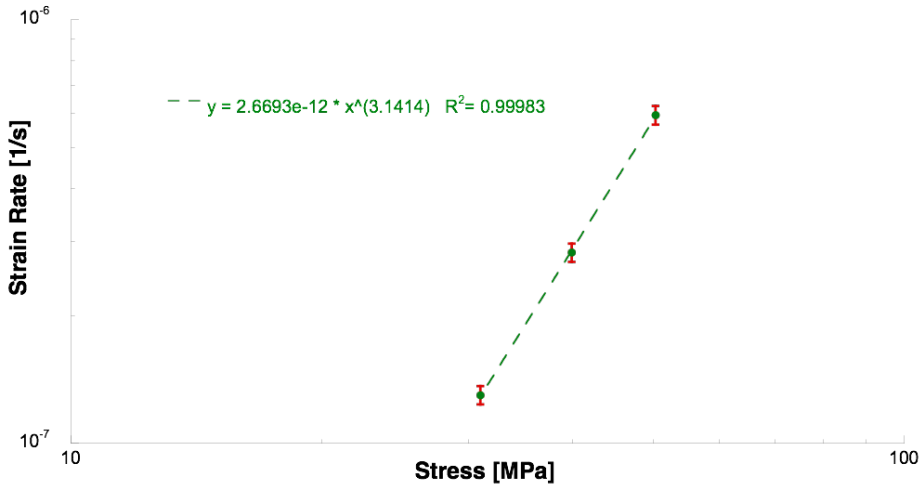

Fig. 27. Strain rate versus stress for the sample tested at the low stress range. Note that the value of R^2 is extremely close to 1 for the power-law fit to the experimental data.

The stress exponent obtained from this fit, which is ~ 3.14 ± 0.05, suggests that dislocation glide is controlling the creep deformation [14], but more information is needed to make a final determination. Samples were also examined after the test to look for slip traces and lattice rotations that could provide insight into the deformation modes. The results for the sample with the dominant single grain are shown in **Fig. 28**.

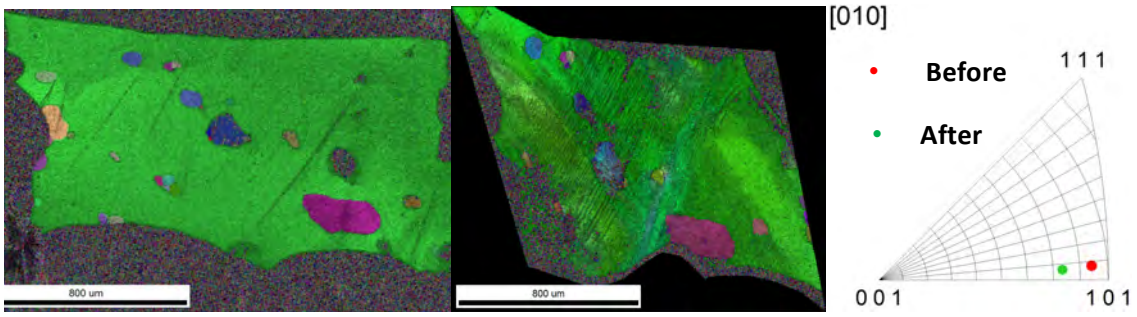

(a) (b) (c)

Fig. 28. Microstructure of the sample with a dominant single grain from observations on a lateral face (a) before the creep test. (b) After the test. (c) Orientation of the loading axis (horizontal) before and after the test.

There was significant deformation on the sample shown in **Fig. 28**, which is consistent with the higher stresses applied. A total permanent strain of about 10.8% was measured for this specimen. Note from **Fig. 28b** that the sample experienced considerable shear deformation, as expected from a single crystal under single slip, and that there were clear slip lines visible on the lateral surface. Slip trace analysis using the EBSD data showed that these traces were consistent with {001} planes, the reported slip plane for UO_2 [15], which suggests inelastic deformation in the samples was dominated by dislocation glide. Furthermore, the results in **Fig. 28c** indicate that the loading axis is rotating towards {001} as deformation proceeds, which is typical of kinematics of glide processes in single crystals experiencing compression between stiff platens [16]. These are strong indications that dislocation glide is controlling the deformation process in these samples. An examination of the bi-crystal sample did not reveal any slip traces; however, it was found that the loading axis of each grain indeed rotated towards {001}, which further

supports the assumption that similar deformation kinematics were taking place in all the samples tested in this work.
Finally, the sample tested at the high stress range had the following stresses applied at each step: 62.8 MPa, 86.0 MPa, and 109 MPa. An analysis similar to that shown in **Fig. 26** indicated that the stress exponent for the high stress range was ~2.9, but with a higher error bar that makes it overlap with the result from the low stress test. Errors are likely to stem from large deformation effects on stress calculations, so a stress exponent of 3.14 was chosen for the model, which will be described in another section.

2.1.2. Microscale Testing Data

Microcantilever beams were fabricated using focused ion beam techniques on a single grain of UO_2 with a surface parallel to the (111) plane, as determined by EBSD. Samples with L/h ~ 7 were used to minimize effects from the substrate on elastic and plastic behavior and loaded using a displacement rate of 10 nm/s until sample fracture under a controlled reducing atmosphere (Ar-5% Hydrogen) to keep O/U ~2. Load-displacement data was collected throughout the test.
The sample was characterized before and after the procedure, using standard SEM imaging in conjunction with EBSD scans to gather orientation data, which was then used to identify crystal orientation parallel to the axis of the beam. An example of the as-machined microcantilever beams and the punch used to load them in-situ is shown in **Fig. 29.**

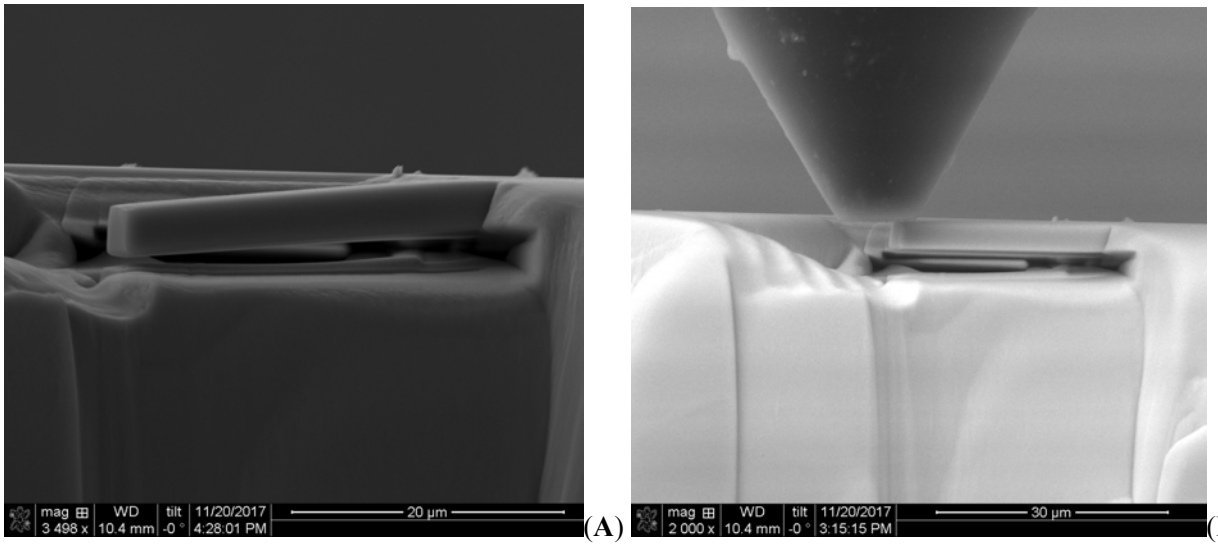

(**A**) (**B**)

Fig. 29. (**A**) Example of a microcantilever beam machined in a single grain of UO_2 using FIB techniques. (**B**) Loading tip positioned at the end of the beam before starting a test.

The EBSD measurements revealed that the sample had a beam axis approximately parallel to ~ <-4 1 3>; the out-of-plane direction is parallel to <111>, and the third one can be obtained as the cross-product of the first two directions. A load-deflection curve for one of these beams is shown in **Fig. 30**.

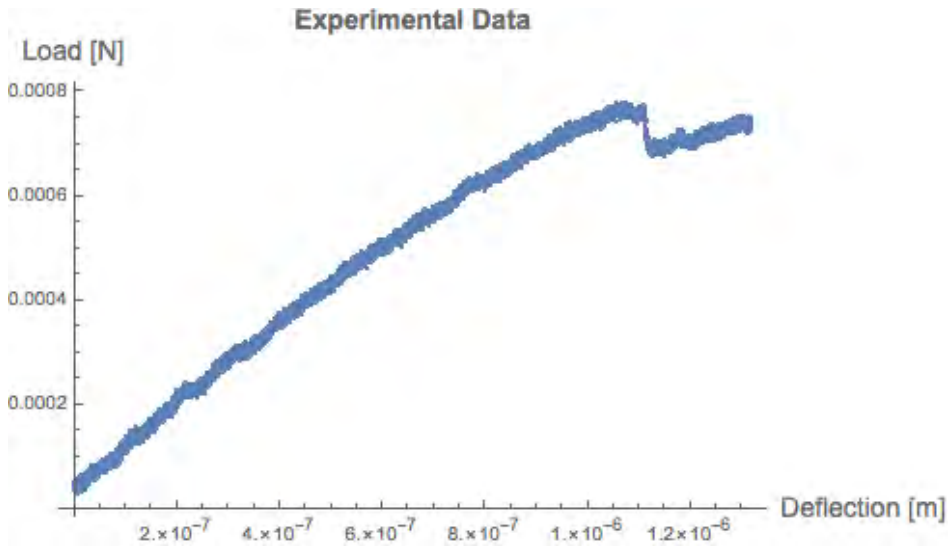

Fig. 30. Load-deflection curved measured at 570 °C for a microcantilever beam parallel to <-4 1 3>.

Additional microcantilever beams were fabricated for further testing using focused ion beam techniques on a single grain of UO_2 with a surface parallel to the (111) plane, as determined by EBSD. Samples that had L/h ~ 8.7 were used to minimize effects from the substrate on elastic and plastic behavior and loaded using a displacement rate of 10 nm/s until sample fracture under a controlled reducing atmosphere (Argon-5% Hydrogen) to keep the oxygen to uranium ratio ~2. Load-displacement data was collected throughout the test. The sample was characterized before and after the procedure, using standard SEM imaging in conjunction with the EBSD scans to gather orientation data, which was then used to identify crystal orientation of the beams parallel to the axis of the beam. One of the as-machined microcantilever beams is shown in **Fig. 31** along with crystal orientation data obtained from EBSD.

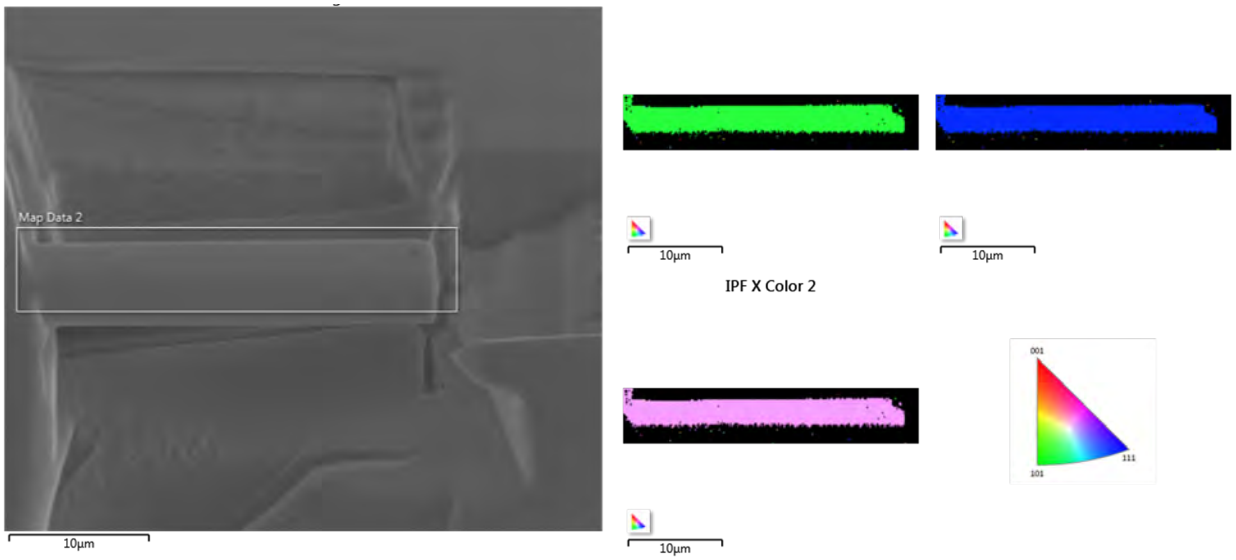

Fig. 31. Example of a microcantilever beam machined in a single grain of UO_2 using FIB techniques and the crystal orientations along the axes of the beam obtained from EBSD.

The EBSD measurements revealed that the sample had a beam axis approximately parallel to ~ <-110> (x direction). The out-of-plane direction is parallel to <111> (z direction), and the third one can be obtained as the cross product of the first two directions,. All these orientations are consistent with the colors shown in the lower half of **Fig. 31**, as per the standard triangle legend in the inset. A load-deflection curve for one of these beams is shown in **Fig. 32**.

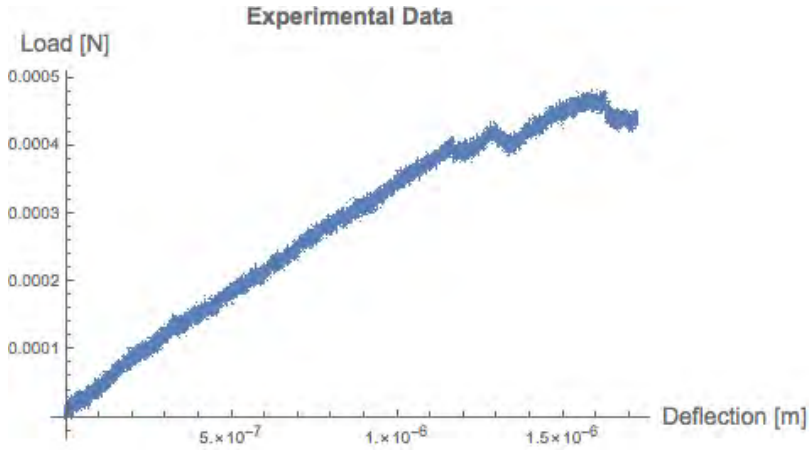

Fig. 32. Load-deflection curved measured at 570 °C for a microcantilever beam parallel to <-110>.

2.2. Formulation of Crystal Plasticity Model

2.2.1. Formulation and Fundamental Assumptions

The stress state for the macroscale samples in this case is simpler than for the cantilever beam testing, but the magnitude of strain the samples experienced was greater than 1% in all cases, which requires the use of large strain kinematics.

Hence, a multiplicative decomposition of the deformation gradient into elastic and inelastic parts was used, i.e., $\mathbf{F}=\mathbf{F}^{el}\mathbf{F}^{in}$ [17-19]. The constitutive model chosen is crystal plasticity with a viscoplastic flow rule, using standard kinematics to relate slip geometry to plastic strain rates (see [17-19] for example). The approach followed here was based on the premise of keeping the models as simple as possible while still being able to capture the behavior observed experimentally, so that the number of material constants can be minimized. This is meant to avoid "overfitting" whereby a model can be made to fit any data if enough constants are available. In this regard, the initial model was based on a viscoplastic flow rule based on a power law [17] and standard crystal elasticity and plasticity kinematics based on the multiplicative decomposition mentioned above. In addition, given the large stiffness of UO_2 the model was taken as rigid plastic, since the elastic strains are expected to be small as compared to the inelastic ones. These assumptions can be represented using the following equations:

$$\dot{\gamma}^{(\alpha)} = \dot{\gamma}_0 \left(\frac{\tau^{(\alpha)}}{\tau_c} \right)^{1/m} Sign\left(\tau^{(\alpha)}\right) \quad (3)$$

$$\tau^{(\alpha)} = \boldsymbol{\sigma} : (\mathbf{b}^{(\alpha)} \otimes \mathbf{n}^{(\alpha)}) \quad (4)$$

$$\mathbf{L}^{(p)} = \sum_{\alpha=1}^{N} \dot{\gamma}^{(\alpha)} \left(\mathbf{b}^{(\alpha)} \otimes \mathbf{n}^{(\alpha)} \right) \quad (5)$$

$$\mathbf{F} = \mathbf{R}^{el}\mathbf{F}^{in} \quad (4)$$

Where $\dot{\gamma}^{(\alpha)}$ is the plastic shear strain rate in slip system α, $\dot{\gamma}_0$ is a reference shear strain rate, m is a strain rate sensitivity exponent, $\tau^{(\alpha)}$ is the resolved shear stress on slip system α, τ_c is the critical value of shear stress needed to produce dislocation motion, $\mathbf{b}^{(\alpha)}$ and $\mathbf{n}^{(\alpha)}$ represent slip direction and plane normal for system α, respectively, $\mathbf{L}^{(p)}$ is the plastic part of the velocity gradient and $\mathbf{R}^{el}$ is a rigid body rotation needed to satisfy appropriate kinematic constraints for the compression test. In that regard, the conditions for compression between stiff platens is that the rate of change of the vector normal to the compression plane is equal to zero. Hence, the rotation of that vector produced by the plastic part of the deformation needs to be balanced by the rotation $\mathbf{R}^{el}$. The corresponding equations can be found in [16].

Another assumption made here is that there is no strain hardening, so τ_c was considered constant, at least initially. The fundamental parameters to fit include $\dot{\gamma}_0$ and τ_c, with m=3.14, as derived from experiments. Slip is assumed to take place on {001}<110> slip systems as per the direct evidence shown in **Fig. 33**.

Given that the stress history and the initial crystal orientation of the samples is known, the equations given above can be integrated in time to obtain strain rates as a function of stress for stage II creep. An explicit time integration algorithm was developed and implemented to calibrate the material constants and to validate the model as discussed in the next section.

2.2.2. Calibration and Validation

The calibration was first performed with the results from the low stress test. Values of $\dot{\gamma}_0$ and τ_c were first found to match the creep strain rates obtained experimentally, and while values for these two parameters were obtained that produced reasonable matches, some of them had differences of 10% or slightly more, which was not optimum and hinted that more physics had to be added. Furthermore, it was also clear that the material parameters from the model without hardening would not be able to match the results from the high stress experiments. Hence, a simple isotropic hardening model was introduced to increase the value of the critical resolved shear stress τ_c needed to produce dislocation motion, whereby τ_c increases as a power-law of the cumulative shear strain in all slip systems [17]. Results are shown in **Fig. 34**.

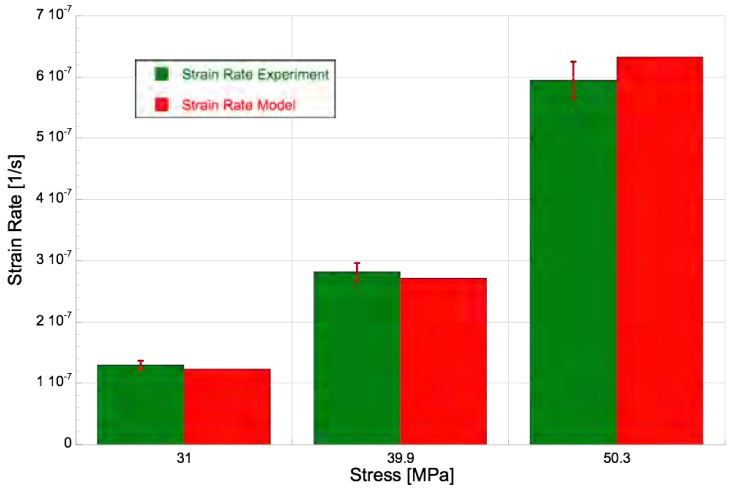

Fig. 33. Comparison between results of calibrated model and experimental strain rates from the low stress range test.

Note from **Fig. 33** that the output of the calibrated crystal plasticity model is within the error bars of the experimental results from the low stress test. Validation of the model was carried out by comparing the predictions of the model to the results from the high stress test; the results are shown in **Fig. 34**.

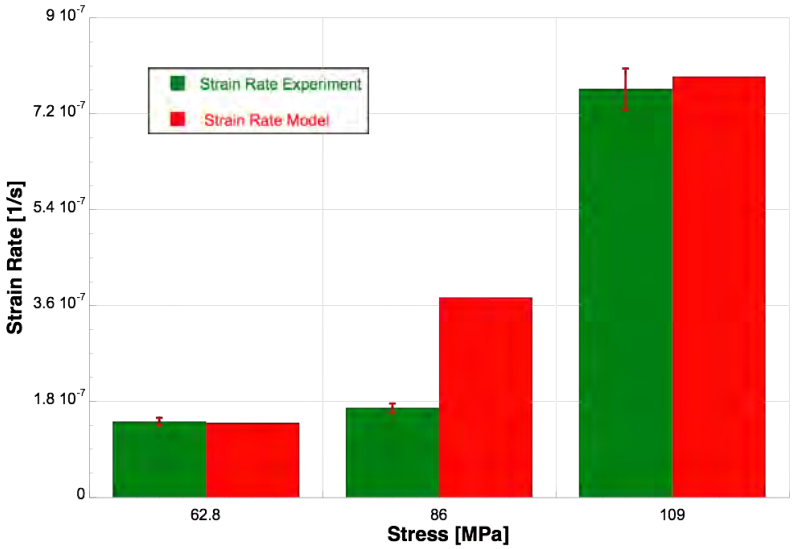

Fig. 34. Comparison between results of calibrated model and experimental strain rates from the high stress test.

Note from **Fig. 34** that the result of the calibrated crystal plasticity model is within the error bars of the experimental results from the high stress test for both the low and high stress values used in the step test. The value of the experimental strain rate for the intermediate stress value for the high stress range seems low for stress exponent used, and the discrepancy is actually consistent with the lower confidence of the power law fit for the experimental data of the high stress test, where $R^2 = 0.886$. The error bars for this experimental data will be reviewed in more detail, but, overall, the calibrated model achieves a very good match with the lower and upper values of stress used, without fitting any parameters, so the model can be considered validated over this range. The following values were obtained: $\dot{\gamma}_0 = 0.083\ s^{-1}$, and initial $\tau_c = 390$ MPa. The exponent of the power-law hardening was ~0.45, close to 0.5, which is consistent with Taylor hardening based on the square root of the dislocation density, which is proportional to the shear strain.

The results indicate the very simple model proposed here was capable of matching the experimental data well with 4 independent parameters, and that dislocation glide controls the creep process while strain hardening plays a role at the sub-grain length scale. Furthermore, the value of critical resolved shear stress obtained would result in large predictions of yield strength for polycrystalline aggregates as compared to experimental values. Finally, evidence of visco-elasto-plastic behavior was present in the transient deformation before stage II creep. This indicates that additional mechanisms are likely at play, and more research might be required to elucidate them.

Similar efforts were carried out to fit models to the results of the microscale tests, as discussed next.

2.3. Formulation of Elasto-Plastic Model for Microcantilever Beams

2.3.1. Formulation and Fundamental Assumptions

There are two aspects to the modeling of the results obtained from bending of microcantilever beams:

a.- Local relationship among slip geometry, stress and plastic strain, i.e., kinematic and kinetic aspects of crystal plasticity at an individual point of the beam.

b.- Global relationship between load and displacement at the point of application of the load and its connection to plastic deformation in the beam.

Aspect (a) relates to purely constitutive modeling, whereas aspect (b) refers to the boundary value problem associated to the testing geometry and procedure chosen.

The constitutive model chosen is crystal plasticity with a viscoplastic flow rule, using standard kinematics to relate slip geometry to plastic strain rates (see [17-19] for example). The approach followed here was also based on the premise of keeping the models as simple as possible while still being able to capture the behavior observed experimentally, to avoid "overfitting." In this regard, the initial model was based on a viscoplastic flow rule based on a power law [17] and standard crystal elasticity and plasticity kinematics, assuming small strains, as expected due to the large stiffness of UO_2. These assumptions can be represented using the following equations:

$$\dot{\gamma}^{(\alpha)} = \dot{\gamma}_0 \left(\frac{\tau^{(\alpha)}}{\tau_c} \right)^{1/m} Sign\left(\tau^{(\alpha)}\right) \tag{6}$$

$$\tau^{(\alpha)} = \boldsymbol{\sigma} : (\mathbf{b}^{(\alpha)} \otimes \mathbf{n}^{(\alpha)}) \tag{7}$$

$$\dot{\boldsymbol{\varepsilon}}^{(p)} = \sum_{\alpha=1}^{N} \dot{\gamma}^{(\alpha)} Sym\left(\mathbf{b}^{(\alpha)} \otimes \mathbf{n}^{(\alpha)}\right) \tag{8}$$

$$\boldsymbol{\sigma} = \mathbf{C} : \left(\boldsymbol{\varepsilon}^{(t)} - \boldsymbol{\varepsilon}^{(p)}\right) \tag{9}$$

Where $\dot{\gamma}^{(\alpha)}$ is the plastic shear strain rate in slip system α, $\dot{\gamma}_0$ is a reference shear strain rate, m is a strain rate sensitivity exponent $\tau^{(\alpha)}$ is the resolved shear stress on slip system α, τ_c is the critical value of shear stress needed to produce dislocation motion, $\mathbf{b}^{(\alpha)}$ and $\mathbf{n}^{(\alpha)}$ represent slip direction and plane normal for system α, respectively, $\dot{\boldsymbol{\varepsilon}}^{(p)}$ is the plastic strain rate tensor, $\boldsymbol{\sigma}$ is the stress tensor, $\mathbf{C}$ is the anisotropic elastic stiffness tensor expressed on the lab coordinate frame, which depends on the crystal orientation of the beam, and $\boldsymbol{\varepsilon}^{(t)}$ is the total strain tensor.

Another assumption made here is that there is no strain hardening, so τ_c will be considered constant, at least initially. The fundamental parameters to fit include $\dot{\gamma}_0$, m, and τ_c. Slip is assumed to take place on {001}<110> slip systems [20] and elastic constants for single crystals are taken from [21], as needed, and corrected for temperature effects using the correlation proposed in [22].

The assumptions associated to the global behavior stem entirely from engineering theory of elasto-plastic beams undergoing small deformations (see [23]). The key relationships here is the one between the bending moment at a given cross-section $M(x)$ and the curvature at that location and the standard kinematic assumption for engineering beams whereby the total strain is assumed to be a linear function of distance from a neutral axis times the curvature κ of that

section, i.e., the inverse of the radius of curvature. The moment curvature relationship for a beam of height 2*h* is given by:

$$\kappa = \frac{M(x)}{EI} + \frac{3}{2h^3}\int_{-h}^{h} y\varepsilon^{(p)}(y)\,dy \quad (10)$$

The kinematic assumption for total axial strains used in bending allows expressing the axial component of equation (9) approximately as:

$$\sigma_{xx} = E(\varepsilon_{xx}^{(t)} - \varepsilon_{xx}^{(p)}) = E(-\kappa y - \varepsilon_{xx}^{(t)}) \quad (11)$$

Where *E* is the equivalent Young's modulus along the crystal direction parallel to the axis of the beam. The use of a beam, hence, allows one to concentrate on stresses and strain along the axial direction of the beam. The fact that the out-plane direction of the beam is parallel to <111> allows neglecting couplings between shear and normal components and 2-D stress fields can be considered (see [24]). An explicit integration scheme was implemented with these equations to relate the applied displacements at the end of the beam to the corresponding load, by assuming that the first time-step was elastic and using discretization in time and space to obtain curvature as a function of position and applied load for a given time. Using the fact that $v''(x) = \kappa(x)$, the deflection v(x) was obtained as a function of the applied load and then the load was obtained by equating the experimental value of the deflection at the end predicted by the model (with load as a parameter).

2.3.2. Calibration and Validation

The first step on the calibration process was to fit a straight line to the linear part of the load-deflection curve and use standard beam theory to deduce an elastic modulus for the material knowing the geometry of the beam. In this case, a beam 24 μm long, 6.33 μm wide and 3.3 μm high was used to obtain the load-deflection data shown in **Fig. 35**. Note the sharp drop in load towards the end, followed by a region where the curve becomes smooth again. This is a clear indication that the micro-beams were experiencing displacement bursts, a phenomenon well-known to occur during testing of samples with small dimensions (see, for example, [25]). Given that the test was done in displacement control, a sudden increase of displacement will produce a sharp drop in load, as observed.

The fit to the linear portion of the load-deflection curve produced a Young's modulus of about 185 GPa, about 5% higher than the prediction from the elastic constants from [21] after the temperature correction from [22]. A plot of the experimental data and the elastic fit to the linear portion of the data is shown in **Fig. 35**.

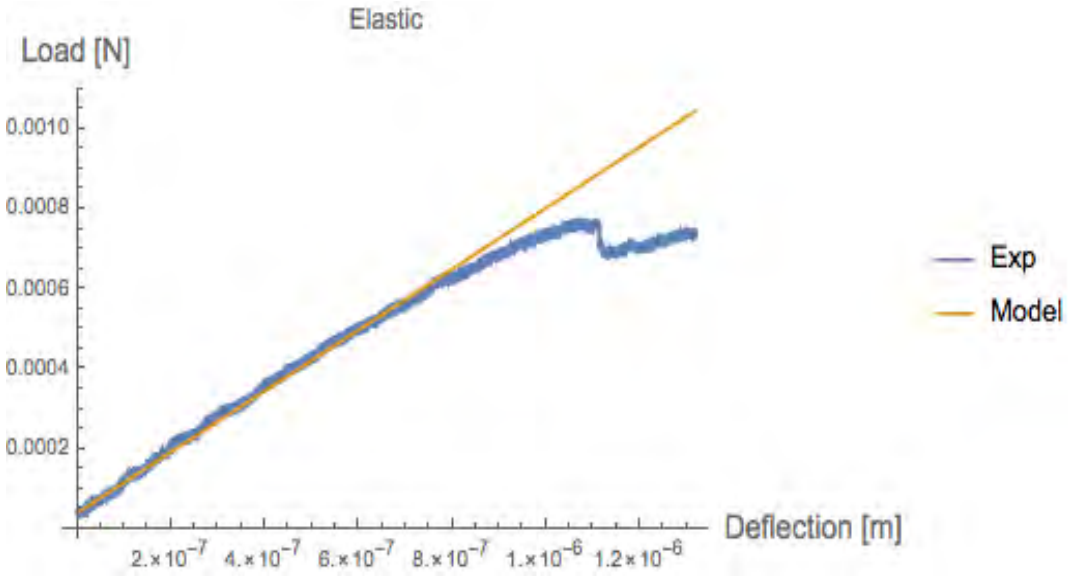

Fig. 35. Elastic fit to the linear portion of the experimental data. The correlation factor R^2=0.9965, indicating an extremely good fit.

The deviation from linearity provides an initial estimation of the value of critical resolved shear stress τ_c needed to start dislocation motion. Then, an iterative process was used to obtain the values of include $\dot{\gamma}_0$ m and τ_c, that produced the best match with the experimental data. Examples of the effects of m on the predicted behavior are shown in **Fig. 36**.

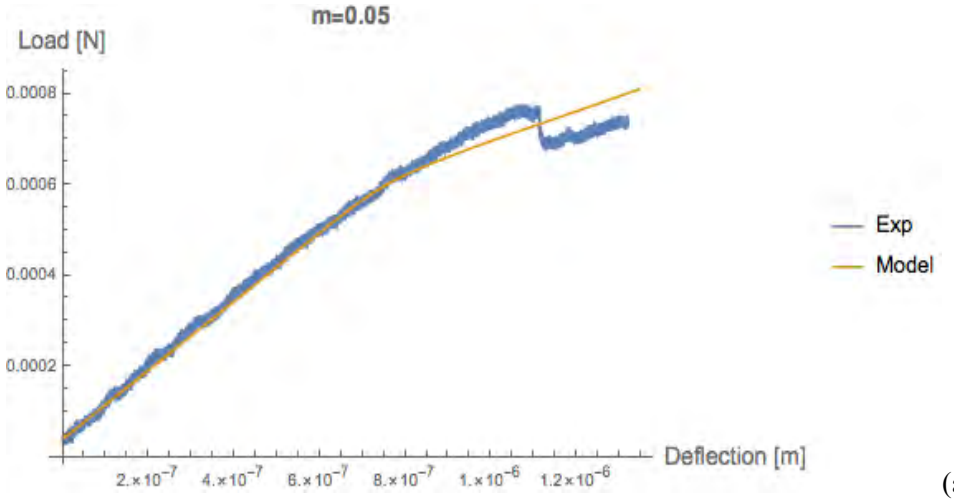

(a)

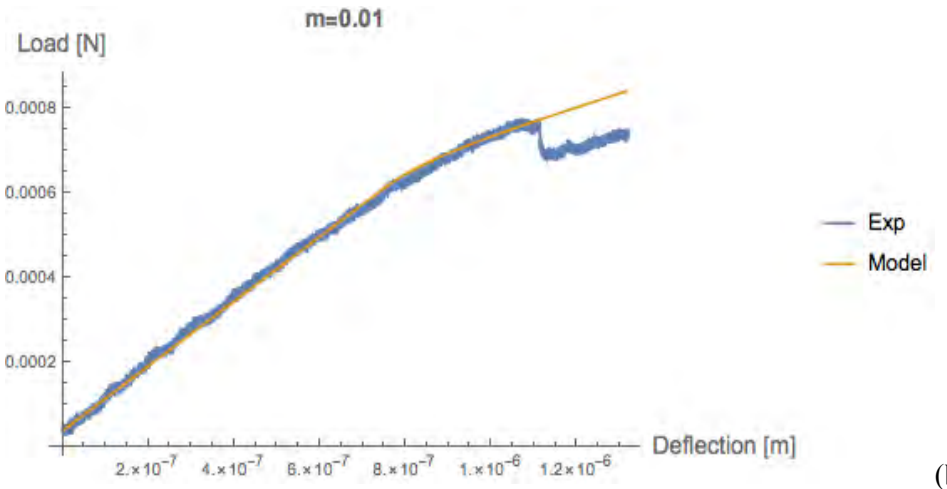

(**b**)

Fig. 36. Effect of strain rate sensitivity on the fit of visco-plastic model to beam results. (**a**) m=0.05, (**b**) m=0.01.

The results indicate the very simple model proposed here was quite capable of matching the experimental data quite well with only 3 independent parameters. The optimum values, which gave results in **Fig 36b**, were include $\dot{\gamma}_0 = 10^{-3}$ s^{-1}, $m = 0.01$ and $\tau_c = 1.05$ GPa. While the value of $\dot{\gamma}_0$ is actually fairly common in the crystal plasticity literature, the value obtained for m has an important consequence: it indicates that a model with extremely low strain rate sensitivity can be used to match the experimental results. This, in turn, strongly suggests that the plasticity for UO_2 at these low temperatures and for the small length scales used is essentially rate independent, and an elastic-perfectly plastic model can in principle be used to model the behavior of the beams. This also indicates that there are not enough distinguishing features in the experimental data to differentiate the simple model used here and others with additional physics.

Finally, the value of τ_c suggests that the experiments at the microscale predict very large macroscale flow stresses (a typical estimate is macro yield strength = $3\tau_c$ = 3.15 GPa!).

The same modeling approach was used for validation of the elastic regime (using additional testing data) without any modifications to the parameters for the visco-plastic model. The flow rule to obtain the plastic shear strain rate for each slip system as a function of the resolved shear stress on that system was expressed using the calibrated constants $=10^{-3}$ s^{-1}, m=0.01 and τ_c=1.05 GPa as:

$$\dot{\gamma}^{(\alpha)} = 10^{-3}\left(\frac{\tau^{(\alpha)}}{1.05\times10^{9}}\right)^{\frac{1}{0.01}} Sign\left(\tau^{(\alpha)}\right) \qquad (12)$$

The same assumptions associated to the global behavior of the micro-beams were used as well, along with the explicit integration technique developed to solve the set of non-linear equations required to obtain the load-deflection curve for the beam.

The first step on the process was to fit a straight line to the linear part of the load-deflection curve and use standard beam theory to deduce an elastic modulus for the material knowing the geometry of the beam. In this case, a beam 24.4 μm long, 5.5 μm wide, and 2.8 μm high was used to obtain the load-deflection data shown in **Fig. 37**. Note the various drops in load towards the end, followed by regions where the curve becomes smooth again. This is a clear indication that the microbeams were experiencing displacement bursts, a phenomenon well-known to occur

during testing of samples with small dimensions (see, for example, [25]). Given that the test was done in displacement control, a sudden increase of displacement will produce a sharp drop in load, as observed. The fact that the beam used here showed more jumps than the one used for calibration might have to do with the fact that the orientation of the beam used for calibration promotes single slip, whereas the $<\bar{1}10>$ axis used for this validation effort promotes multiple slip, according to calculations of Schmid factor for {001}<110> slip. It is possible that the individual jumps that can be seen on **Fig. 37** might correspond to activation of different slip systems. However, displacement bursts can occur over the same slip systems as the deformation proceeds [26], so more information would be required to assess the slip systems responsible for the jumps. The fit to the linear portion of the load-deflection curve produced a Young's modulus of about 162 GPa, about 7% lower than the prediction from the elastic constants from [21] after the temperature correction from [22]. A plot of the experimental data and the elastic fit to the linear portion of the data is shown in **Fig. 37**.

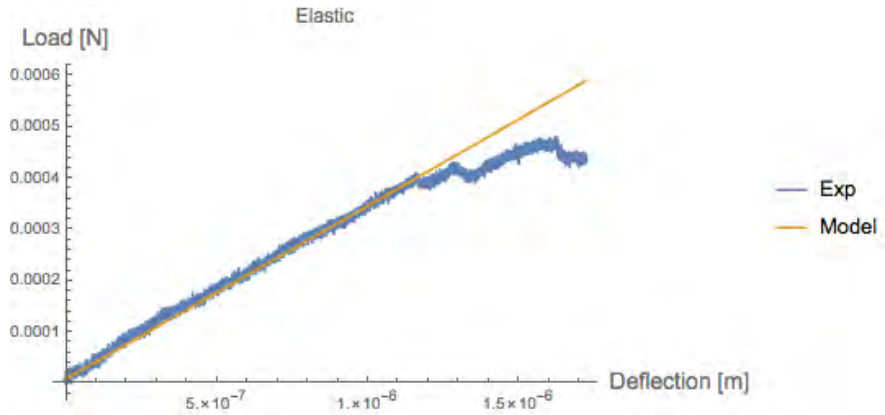

Fig. 37. Elastic fit to the linear portion of the experimental data. The correlation factor R^2=0.9934, indicates an extremely good fit to the linear behavior.

One issue with the presence of load jumps in the curve, as a result of the displacement bursts, is that continuum models are ill suited to capture them. However, validation can still be carried out by removing the effects of the displacement bursts from the experimental data, given that the crystal plasticity model used here is mostly concerned with the rates of plastic deformation rather than the total plastic strain. Hence, only the deformation that would have taken place without the jumps, i.e., the one that corresponds more closely to the proposed model, is used to make meaningful comparisons. The corrected curve is shown in **Fig. 38**.

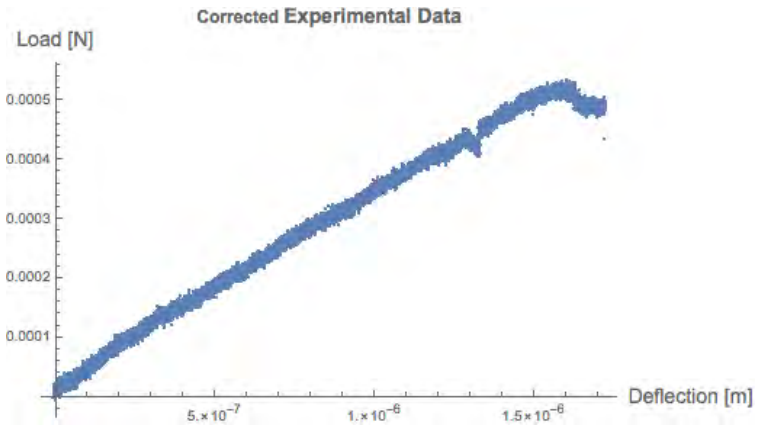

Fig. 38. Corrected experimental data after removing load jumps.

A comparison between the predicted load-deflection curve using the calibrated visco-plastic model, as is, and the corrected experimental data is shown in **Fig. 39**.

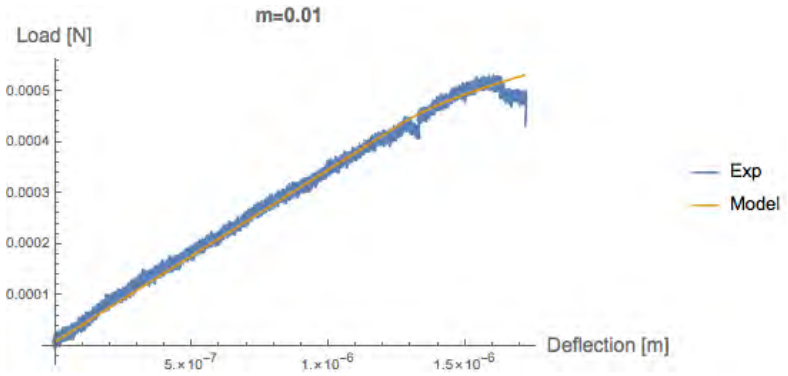

Fig. 39. Comparison of predicted (model) and corrected experimental load-deflection curves.

The results indicate the very simple model proposed here was capable of matching the experimental data quite well for a different crystal orientation than that used to calibrate the model, without any adjusted on the visco-plastic parameters. This provides further evidence that plasticity for UO_2 at these low temperatures and for the small length scales used is essentially rate independent, and an elastic-perfectly plastic model can in principle be used to model the behavior of the beams. The presence of load jumps also indicates that the specimens are small enough to experience displacement bursts, likely due to bursts of dislocation motion. However, it is interesting that the sample dimensions (cross-sections of about a few μm's) used here are larger than those for which this phenomenon has been observed in metals (submicron, ~100 nm). This might be related to the low volumetric density of defects expected in UO_2, so that for the dimensions used here, the surface becomes the most important source of defects, leading to dislocation nucleation from the surface. The fact that bending stresses are largest at the surface favors this interpretation. The hypothesis that dislocations nucleate from the surface is also consistent with the fact that the experimental results imply that the UO_2 micro-beams are experiencing plasticity in tension in their upper fibers, which is certainly unexpected at the temperatures used for the test. The low density of volumetric defects might also explain why the samples did not break in the tension side of the beams and preferred to slip instead. Additional experiments using other techniques, e.g., micro-pillar compression, could be helpful to determine if there is a tension compression asymmetry on the behavior of the material that might skew the result towards higher values of the critical resolved shear stress.

Finally, some comments on the elastic behavior are also important here. The effective Young's modulus on the {111} plane of a cubic single crystal should be isotropic for direction on this plane [25], i.e., in theory all the beams used in the experiments for calibration and validation should produce the same value of Young's modulus. It was found that the aspect ratio of the beam had an effect on the value of effective Young's modulus derived from the experiments. Scatter was high at aspect ratios L/h ~ 5, and the scatter went down when the aspect ratio increased above 7. However, there were other sources of scatter that are yet to be elucidated, particularly given that the effect of substrate should be small for $L/h \geq 5$, with 5 being the initial target in this work to keep the beams inside single grains.

Student Status

Two PhD students were supported under this project. Benjamin Shaffer, at ASU has already passed his qualifying exam and is finishing writing his dissertation, and he is expected to graduate on summer 2018. David Frazer, was supported at UC Berkeley. Two MS students were supported at ASU, Robert McDonald, now at Honeywell Aerospace, and Bowen Gong, and they graduated in 2015. B. Gong went on to become a PhD student at RPI working on another NEUP project. A postdoc at ASU, H. Lim, was also partially supported under this project and he is now at Intel. Finally, two undergraduate students worked at ASU under this project, K. Roney, now at APS, and Y. Tong, who will be graduating in Spring 2018.

Dissemination

Conference Presentations

Rudman, K., Lim, H., McDonald, R.E., Peralta, P., Byler, D., and McClellan, K. "Correlations between Grain Boundary Texture and Grain Growth in d-UO_2". Contributed Talk. TMS Annual Meeting, March 2014, San Diego, CA.

McDonald, R.E., Frazer, D., Lim, H., Rudman, K., Hosemann, P., and Peralta, P. "Mechanical Behavior of UO_2 at Sub-grain Length Scales". Poster presentation. AFC Meeting. Idaho National Laboratory, Idaho Falls, ID. August 2014.

Shaffer, B., Lim, H.C., McDonald, R., Gong, B., Frazer, D., Hosemann, P., and Peralta, P. "Mechanical Behavior of UO_2 at Sub-Grain Length Scales: A Quantification of Creep Properties via High Temperature Mechanical Testing." Contributed technical presentation. TMS Annual Meeting & Exhibition, February 2016, Nashville, TN.

Gong, B., Lim, H.C., Shaffer, B., Frazer, D., Hosemann, P., and Peralta, P. "Finite Element Analysis of Micro-Cantilever Beam Experiments in UO_2." Contributed technical presentation. TMS Annual Meeting & Exhibition, February 2016, Nashville, TN.

D. Frazer, H. Lim, B. Shaffer, B. Gong, P. Peralta, and P. Hosemann, "Microscale Mechanical Testing of UO_2 Fuel at Elevated Temperatures." Contributed Talk. TMS Annual Meeting and Exhibition, Nashville, 2016.

Shaffer, B., Lim, H.C., McDonald, R.E., and Peralta, P. "Mechanical Behavior of UO_2 at Sub-Grain Length Scales: A Quantification of Creep Properties via High Temperature Mechanical Testing." Contributed technical presentation. ASME Annual International Mechanical Engineering Congress and Exposition, November 2016, Phoenix, AZ.

Shaffer, B., Lim, H.C., McDonald, R.E., Gong, B., Frazer, D., Hosemann, P., and Peralta, P. "Characterization of High Temperature Deformation Behavior at the Grain Level in UO_2 via Electron Backscatter Diffraction." Contributed technical presentation. TMS Annual Meeting & Exhibition, February 2017, San Diego, CA.

Frazer, D., Shaffer, B., Roney, K., Lim, H.C., Gong, B., Hosemann, P., and Peralta, P. "Small-Scale Mechanical Testing of UO_2." Contributed technical presentation. ANS Annual Meeting, June 2017, San Francisco, CA.

Rudman, K., Shaffer, B., Lim, H.C., McDonald, R.E., and Peralta, P. "Correlation between Grain Size Distribution and Grain Boundary Character in Polycrystalline Uranium Dioxide." Contributed technical presentation. ANS Annual Meeting, June 2017, San Francisco, CA.

D. Frazer, B. Shaffer†, P. Peralta, and P. Hosemann, "Effects of High Temperature Pre-strain on Hardness and Creep Behavior of UO_2 between 25 and 500 °C: A Nanoindentation Study." American Nuclear Society Winter Meeting, Washington DC, 2017.

Shaffer, B., and Peralta, P. "Characterization of Intra-granular Creep Deformation in Uranium Dioxide Using Electron Backscatter Diffraction and Electron Channeling Contrast Imaging." Contributed technical presentation. TMS Annual Meeting & Exhibition, February 2018, Phoenix, AZ.

Shaffer, B., Frazer, D., Hosemann, P., and Peralta, P. "Mechanical Behavior of UO_2 at Sub-grain Length Scales". Technical presentation. AFC Meeting, University of New Mexico, Albuquerque, NM. December 2017.

Articles

H. Lim, K. Rudman, K. Krishnan, R. McDonald, P. Dickerson, B. Gong, and P. Peralta, "*Effects of microstructural constraints on the transport of fission products in uranium dioxide at low burnups*." Journal of Nuclear Materials, 477, (2016), p. 24-36.

Rudman, K., Shaffer, B., Lim, H.C., McDonald, R.E., and Peralta, P. "*Correlation between Grain Size Distribution and Grain Boundary Character in Polycrystalline Uranium Dioxide*." ANS Transactions, 2017. **116(1)**: p. 488-491. 0003-018X (ISSN), 1252341 (OCLC).

Frazer, D., Shaffer, B., Roney, K., Lim, H.C., Gong, B., Hosemann, P., and Peralta, P. "*Small-Scale Mechanical Testing of UO_2.*" Transactions of the American Nuclear Society, 2017. **116(1)**: p. 485-487. 0003-018X (ISSN), 1252341 (OCLC).

B. Shaffer†, R. McDonald, H. Lim, and P.D. Peralta, "Mechanical behavior of UO_2 at sub-grain length scales: A quantification of creep properties via high temperature mechanical testing." ASME International Mechanical Engineering Congress and Exposition, Proceedings (IMECE) Volume 9, 2016 (published 2017). Code 128056. **DOI**: 10.1115/IMECE2016-67772.

References

1. Higgs, J.D., Lewis, B.J., Thompson, W.T., and He, Z., *A conceptual model for the fuel oxidation of defective fuel*, Journal of Nuclear Materials, 2007. **366**(1-2): p. 99-128.
2. Joung, C.Y., Lee, S.C., Kim, S.H., Kim, H.S., and Sohn, D.S., *Fabrication method for UO_2 pellets with large grains or a single grain by sintering in air*, Journal of Nuclear Materials, 2008. **375**(2): p. 209-212.
3. Mansouri, M.A. and Olander, D.R.: Journal of Nuclear Materials, 1998. **254**: p. 22-33.
4. Assman, H., Dörr, W. and Peehs, M.: J. Nuc. Mat., 1986. **140**: p. 1-6.
5. Di Maio, D. and Roberts, S.G.: Journal of Materials Research, 2005. **20**(2): p. 299-302.
6. Armstrong, D.E.J., Wilkinson, A.J. and Roberts, S.G.: Journal of Materials Research, 2009. 24(11): p. 3268-3276.

7. Varshney, D. and Shriya, S.: Journal of Nuclear Materials, 2013. **440**(1-3): p. 344-365.
8. Mansour, H., Guyon, J., Crimp, M.A., Gey, N., Beausir, B., Maloufi, N., Scr. Met., 84-85 (2014), p. 11-14.
9. Armstrong, W.A., Causey, A.R., Sturrock, W.R., J. Nuc. Mat., 19 (1966), p. 42-49
10. ASTM, C1430-07. 2011, ASTM International.
11. Keller, R.J., Mitchell, T.E., and Heuer, A.H., Acta Metall., 36:4 (1988), p. 1061-1071.
12. Keller, R.J., Mitchell, T.E., and Heuer, A.H., Acta Metall., 36:4 (1988), p. 1073-1083.
13. Kingery, W.D., Bowen, H.K. and Uhlmann, D.R., *Introduction to Ceramics*. Second Edition ed. 1976, New York: John Wiley & Sons.
14. Cannon, W.R. and Langdon, T.E., *Review. Creep of Ceramics. Part 1: Mechanical Characteristics*, J. Mater. Sci., 1983. **18**: p. 1-50.
15. Keller, R.J., Mitchell, T.E. and Heuer, A.H., *Plastic Deformation in Nonstoichiometric UO_{2+x} Single Crystals - II. Deformation at High Temperatures*, Acta Metall., 1988. **36**(4): p. 1061-1071.
16. Havner, K.S., *Finite Plastic Deformation of Crystalline Solids*. Cambridge Monographs on Mechanics and Applied Mathematics, ed. G.K. Batchelor and L.B. Freund. 1992, Cambridge: Cambridge University Press.
17. Asaro, R.J., *Micromechanics of Crystals and Polycrystals*, Adv. Appl. Mech., 1983. **23**: p. 1-115.
18. Bassani, J.L., *Plastic Flow of Crystals*, Adv. Appl. Mech., 1994. **30**: p. 191-258.
19. Hill, R. and Havner, K.S., *Perspectives in the Mechanics of Elastoplastic Crystals*, J. Mech. Phys. Solids, 1982. **30**(1/2): p. 5-22.
20. Olander, D., *Fundamental Aspects of Nuclear Reactor Fuel Elements*. 1976, Oak Ridge: U.S. Department of Commerce, National Technical Information Service.
21. Fritz, I.J., *Elastic properties of UO_2 at high pressure*, Journal of Applied Physics, 1976. **47**(10): p. 4353.
22. Stehle, H., Assman, H. and Wunderlich, F., *Uranium Dioxide Properties for LWR Fuel Rods*, Nuclear Engineering and Design, 1975. **33**: p. 230-260.
23. Srinivasa, A.R. and Srinivasa, S.M., *Inelasticity of Materials: an Engineering Approach and a Practical Guide*. 2009, Singapore: World Scientific Publishing Company.
24. Ting, T.C.T., *Anisotropic Elasticity: Theory and Applications*. 1996, New York: Oxford University Press.
25. Greer, J.R., Oliver, W.C. and Nix, W.D., *Size Dependence of Mechanical Properties of Gold at the Micron Length Scale in the Absence of Strain Gradients*, Acta mater., 2005. **53**: p. 1821-1830.
26. Li, L., Anderson, P., Lee, M., Bitzek, E., Derlet, P., and Swygenhoven, H., *The stress–strain response of nanocrystalline metals: A quantized crystal plasticity approach*, Acta Materialia, 2009. **57**(3): p. 812-822.
27. Nye, J.F., *Physical Properties of Crystals*. 1985, Oxford: Oxford University Press.
28. Iltis, X., Ben Saada, M., Mansour, H., Gey, N., Hazotte, A., Maloufi, N., Jour. Nucl. Mat., 474 (2016), p. 1-7.